

10 MK GAS IN M17 AND THE ROSETTE NEBULA: X-RAY FLOWS IN GALACTIC H II REGIONS

LEISA K. TOWNSLEY,¹ ERIC D. FEIGELSON,^{1,2} THIERRY MONTMERLE,² PATRICK S. BROOS,¹ YOU-HUA CHU,³
AND GORDON P. GARMIRE¹

Received 2003 January 10; accepted 2003 April 28

ABSTRACT

We present the first high spatial resolution X-ray images of two high-mass star forming regions, the Omega Nebula (M17) and the Rosette Nebula (NGC 2237–2246), obtained with the *Chandra X-Ray Observatory* Advanced CCD Imaging Spectrometer instrument. The massive clusters powering these H II regions are resolved at the arcsecond level into more than 900 (M17) and 300 (Rosette) stellar sources similar to those seen in closer young stellar clusters. However, we also detect soft diffuse X-ray emission on parsec scales that is spatially and spectrally distinct from the point-source population. The diffuse emission has luminosity $L_X \simeq 3.4 \times 10^{33}$ ergs s⁻¹ in M17 with plasma energy components at $kT \simeq 0.13$ and $\simeq 0.6$ keV (1.5 and 7 MK), while in Rosette it has $L_X \simeq 6 \times 10^{32}$ ergs s⁻¹ with plasma energy components at $kT \simeq 0.06$ and $\simeq 0.8$ keV (0.7 and 9 MK). This extended emission most likely arises from the fast O star winds thermalized either by wind-wind collisions or by a termination shock against the surrounding media. We establish that only a small portion of the wind energy and mass appears in the observed diffuse X-ray plasma; in these blister H II regions, we suspect that most of it flows without cooling into the low-density interstellar medium. These data provide compelling observational evidence that strong wind shocks are present in H II regions.

Subject headings: H II regions — open clusters and associations: individual (NGC 2244, NGC 6618) — stars: early-type — stars: pre-main-sequence — X-rays: stars

1. INTRODUCTION

One of the great successes in astrophysics during the mid-20th century was the development of a detailed explanation for H II regions and other bright emission-line nebulae (Menzel 1937; Strömberg 1939; Aller 1956). A hot star with strong ultraviolet radiation produces an expanding ionization front that spreads into the surrounding medium. Early studies concentrated on the ionization front, its associated shock, and various other considerations such as magnetic fields, turbulence, dynamical instabilities, and radiation pressure on dust particles (Mathews & O’Dell 1969).

These efforts omitted the potential effects of the powerful winds of OB stars, which were not known until the discovery of ultraviolet P Cygni profiles by Morton (1967). Winds make a relatively small contribution to the overall energy budget of H II regions: the wind mechanical luminosity ranges from 0.3% (B0 V) to 2% (O4 V) of the ionizing continuum luminosity (Panagia 1973; Howarth & Prinja 1989). However, they can easily dominate the dynamics of the nebula by evacuating a hot cavity with characteristic temperatures of $T \sim 10^7$ – 10^8 K and producing two-fluid shocks that lie within the ionization shocks in the cooler $T \sim 10^4$ K H II region (e.g., Pikel’ner 1968; Dyson & de Vries 1972; Weaver et al. 1977). See Lamers & Cassinelli (1999) for details of these models and a historical review of stellar wind studies.

In the interstellar bubble model developed by Weaver et al. (1977), a single 10^6 yr old O7 star with a terminal wind velocity $v_w = 2000$ km s⁻¹ and mass-loss rate $\dot{M} = 1 \times 10^{-6} M_\odot$ yr⁻¹, surrounded by a uniform interstellar medium of density $n_0 = 1$ cm⁻³, will have an innermost region where

the wind freely expands and cools, followed by a hot $T \sim 10^6$ K region starting at the wind termination shock 6 pc from the star and extending to an outer shock at 27 pc. This X-ray-emitting region occupies most of the volume of the bubble and consists mostly of evaporated interstellar material rather than wind material. Outside this hot region lies a thin shell of swept-up interstellar matter at $T \simeq 10^4$ K, beyond which lies the much larger standard photoionized H II region.

The fate of OB winds in H II regions may not be as simple as described in the Weaver et al. interstellar bubble model. The windswept bubble can be larger or smaller than the ionized H II region, and nonadiabatic dissipation due to conduction, mixing, turbulence, and magnetic fields at the shock fronts may affect the properties of the coronal region (Capriotti & Kozminski 2001). Another possibility is that the winds are slowed by the entrainment of dense clumps of interstellar matter before the termination shock. In such mass-loaded stellar winds, extensively studied by Dyson and his collaborators (Pittard, Hartquist, & Dyson 2001 and references therein), the flow is heated to X-ray temperatures closer to the star and the outer shock is weaker. Finally, it is possible that no X-ray emission will emerge at all if the surrounding medium is too fragmented (McKee, Van Buren, & Lazareff 1984) or wind energy is slowly dissipated in a thick turbulent mixing layer (Kahn & Breitschwerdt 1990).

Despite three decades of theoretical discussions of hot cavities produced by OB stellar winds, only a few detailed predictions of observable X-ray properties of the shocked wind have been made. Dorland & Montmerle (1987) investigated the dissipation of a $v_w = 1000$ km s⁻¹ O star wind, including conduction processes, predicting an X-ray to wind kinetic luminosity ratio $L_X/L_w \sim 10^{-5}$ and X-ray temperatures around 2 keV (23 MK) with a nonthermal hard-energy tail. Comerón (1997) presents a two-dimensional hydrodynamic model of an O star residing near the edge of

¹ Department of Astronomy and Astrophysics, 525 Davey Laboratory, Pennsylvania State University, University Park, PA 16802.

² Service d’Astrophysique, Centre d’Études de Saclay, 91191 Gif-sur-Yvette, France.

³ Astronomy Department, University of Illinois at Urbana-Champaign, 1002 West Green Street, Urbana, IL 61801.

an interstellar cloud, showing the evolution of X-ray morphology as the wind cavity produces a blowout into the diffuse interstellar medium. Strickland & Stevens (1999) give a hydrodynamic calculation for a very young ($t \sim 10^4$ yr) O star completely embedded in a dense cloud and find that, while most of the emission from the wind termination shock is in the EUV band, the windswept interior emits X-rays up to several keV in temperature. Cantó, Raga, & Rodríguez (2000) present a three-dimensional hydrodynamic calculation of a rich ensemble of O stars allowing for mass loading, wind collisions, and shocks, but without an encounter with a surrounding cloud. This results in an inhomogeneous X-ray structure with $L_X \simeq 6 \times 10^{35}$ ergs s^{-1} and $T \simeq 2 \times 10^7$ K concentrated in the inner $r \simeq 0.3$ pc of the stellar cluster.

On the observational side, until very recently there had been no unambiguous report of diffuse X-ray emission from H II regions, although it has been detected around some isolated Wolf-Rayet (W-R) stars, within planetary nebulae, and in starburst superbubbles (see reviews by Mac Low 2000; Chu, Guerrero, & Gruendl 2003; Chu 2003; Chu, Gruendl, & Guerrero 2003). Using the *Einstein Observatory*, Seward & Chlebowski (1982) found extended soft X-rays over tens of parsecs in the Carina Nebula with $L_X \simeq 2 \times 10^{35}$ ergs s^{-1} , in addition to a score of individual OB/W-R stellar sources. However, this is a large and old star formation region with many supergiants, so it is possible that this extended emission is dominated by past supernova remnants (SNRs). Leahy (1985) suggested a diffuse origin for emission within the Rosette Nebula seen with *Einstein*, further discussed by Dorland & Montmerle (1987), but a later higher resolution *ROSAT* study concluded that this unresolved component was due to the integrated emission from many lower mass pre-main-sequence stars (Berghöfer & Christian 2002). In an *Einstein* survey of LMC H II regions, Chu & Mac Low (1990) found several with X-ray emission at levels around 10^{35} – 10^{36} ergs s^{-1} , an order of magnitude higher than expected from the wind-shocked bubble, which they attributed to off-center SNRs hitting the outer shells.

The difficulties encountered in past efforts to detect the $T \sim 10^6$ – 10^7 K gas in H II region wind-blown bubbles arise from the complex environment in the X-ray band. A high-mass star forming region (HMSFR) 1–10 pc in extent will have thousands of lower mass pre-main-sequence stars each emitting 10^{28} – 10^{31} ergs s^{-1} , individual OB and W-R stars each emitting 10^{30} – 10^{34} ergs s^{-1} , possibly SNRs and superbubbles emitting 10^{34} – 10^{37} ergs s^{-1} , and possibly X-ray binary systems from past episodes of star formation each emitting 10^{33} – 10^{40} ergs s^{-1} (Feigelson 2001). These observational difficulties are largely overcome with the *Chandra X-Ray Observatory*, where the mirrors give unprecedented subarcsecond spatial resolution and the Advanced CCD Imaging Spectrometer (ACIS) instrument has the very low background necessary to study faint diffuse emission. *Chandra* thus provides the best opportunity to date to resolve the extended, low surface brightness wind-blown bubbles from the plethora of compact stellar X-ray sources expected in HMSFRs. Several reports of wind-generated diffuse X-ray emission from H II regions are thus emerging from recent *Chandra* observations.

We report here on *Chandra* studies of two bright, nearby ($d \sim 1.5$ kpc), and well-studied H II regions: M17 and the Rosette Nebula. In M17, we show that the *Chandra* image reveals strong diffuse X-rays both within and expanding

asymmetrically from the stellar cluster, in addition to several hundred young stars. Preliminary results for M17 were presented in Townsley et al. (2003). In the Rosette, we see relatively faint X-ray emission suffusing the hollow core of the H II gas, together with a rich stellar population.⁴ These observations, and the astrophysical analysis derived from them, represent the strongest observational evidence to date for X-ray emission from the wind-blown cavities of H II regions; the morphological and spectral properties of the hot plasma should constrain some of the theoretical uncertainties concerning the fate of OB winds and the resulting evolution of H II regions.

The paper starts with an overview of each H II region (§ 2) and then presents our observations and results from data analysis (§ 3). The complex morphologies of the X-ray images are reviewed in § 4, and the physical nature of the emitting gas is derived in § 5. Several possible origins of the diffuse emission are considered in § 6 and the wind shock model is discussed in more detail in § 7. The two regions studied here are placed into a wider context in § 8. The paper ends with general comments about the fate of O star winds in H II regions (§ 9).

2. OBSERVATIONAL BACKGROUND ON THE H II REGIONS

2.1. M17

The H II region M17 [= Omega Nebula = W38, at (l, b) = ($15^\circ 1', -0^\circ 7'$)] is visually very bright and has been extensively studied for two centuries. It is illuminated by the massive stellar cluster NGC 6618, the center of which consists of a ring of seven O stars $\sim 1'$ in diameter located behind substantial obscuring material, with $A_V \sim 8$ mag (Hanson, Howarth, & Conti 1997). The cluster core radius is ~ 5.5 (2.6 pc), and its outer radius is ~ 12.5 (5.8 pc) (Lyngå 1987). The earliest O stars are an O4-O4 binary called Kleinmann's Anonymous Star (Kleinmann 1973). The nebula is the second brightest thermal radio source in the sky (after Orion A) and is situated at the edge of a massive and dense molecular cloud; its appearance varies significantly as a function of wavelength because of spatially complex extinction.

A global geometric model of the M17 complex is presented by Tsivilev & Krasnov (1999, their Fig. 4); they note its similarity to the pressure-driven bubble model of Clayton et al. (1985), who in turn note that the highly asymmetric bubble they see agrees with the models of Dyson (1977) and Różyczka & Tenorio-Tagle (1985) for the formation of a wind-blown bubble in the density gradient present at the edge of a molecular cloud. Tsivilev & Krasnov (1999) describe a bowl-shaped region ~ 2 pc across and expanding westward into the molecular cloud, with a much larger, unobscured optical H II region spreading into the low-density medium at the eastern edge of the cloud. The complex resembles the Orion Nebula/KL region seen nearly edge-on (Meixner et al. 1992): the bowl-shaped ionization blister is eroding the edge of the clumpy molecular cloud and triggering massive star formation, as evidenced by an ultracompact H II region and luminous protostars. Velocity studies show an ionized shell in the middle of the nebula

⁴ See the press release at http://chandra.harvard.edu/press/01_releases/press_090601wind.html.

with a diameter of 8 pc ($\sim 17'$; Clayton et al. 1985). The ionization front encounters the molecular cloud at two photo-dissociation regions, known as the northern and southern bars, about $20'$ in length and at an apparent angle of $\sim 45^\circ$ to each other. These dominate the radio continuum and emission-line images of the region (Fig. 1a). The bowl is oriented somewhat past edge-on to our line of sight, with the blowout moving away from us.

In the radio band unaffected by extinction, low-resolution and low-frequency studies with the Very Large Array show an optically thick, bright region associated with bright $H\alpha$ emission truncated abruptly to the west. This is embedded

within an optically thin region extending over $30' \times 40'$ (~ 14 pc \times 19 pc) that represents the full extent of ionized material (Subrahmanyan & Goss 1996). The electron temperature is $T_e \sim 8000$ K. At higher resolution and frequencies, where the $H\ II$ gas is optically thin, the emission is dominated by the bars (Fig. 1a; Felli, Massi, & Churchwell 1984; Brogan & Troland 2001). The gas in the bars has electron density $n_e \sim 10^3$ cm $^{-3}$ but is not uniform, with clumps of higher density. The Lyman continuum flux necessary to excite the bars is consistent with the ultraviolet emission from the O4-B0 stellar cluster, confirming a simple photoionization origin for the radio-emitting gas.

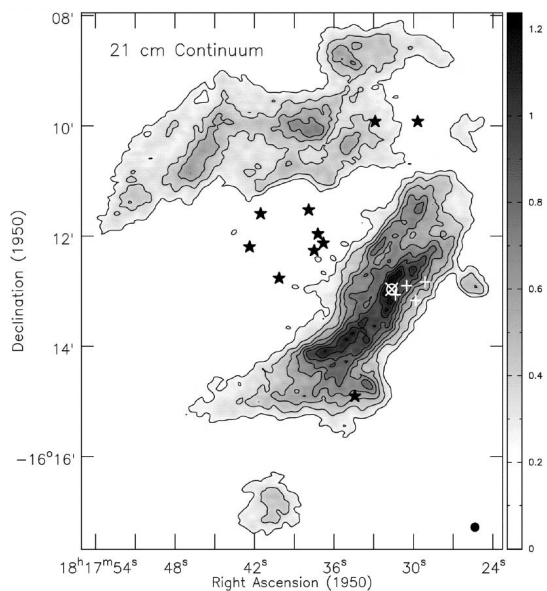


FIG. 1a

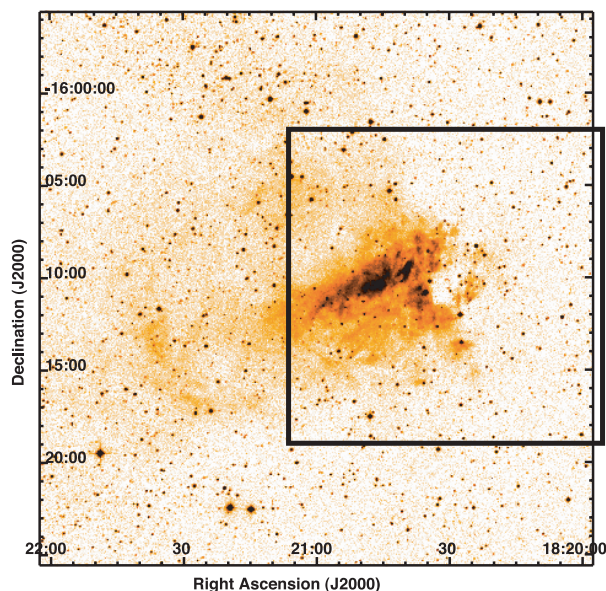


FIG. 1b

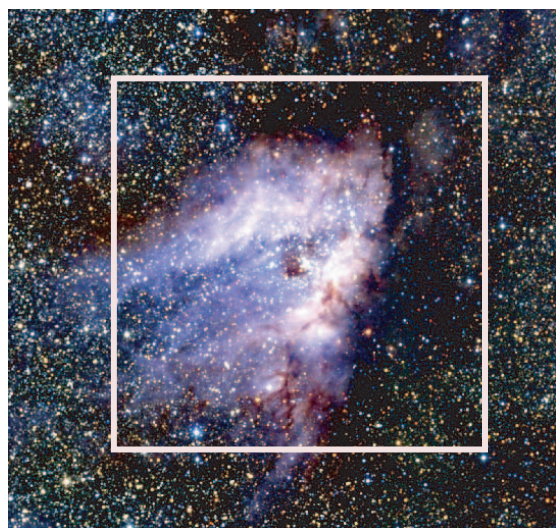


FIG. 1c

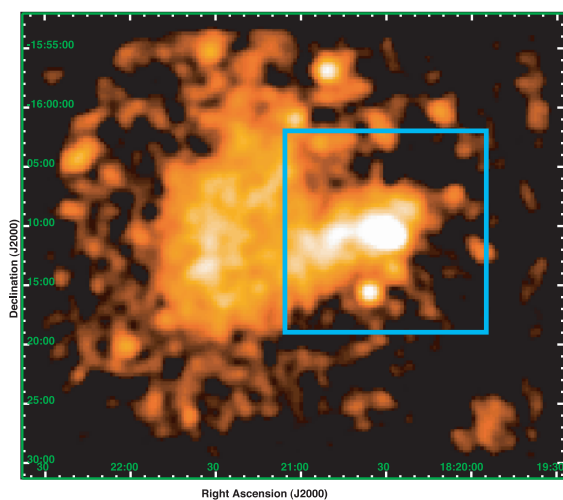


FIG. 1d

FIG. 1.—Multiwavelength views of M17. (a) Radio continuum map showing $H\ II$ gas with respect to the brightest O stars (filled stars), the embedded ultracompact $H\ II$ region (circle), and nearby molecular masers (pluses and cross) from Brogan & Troland (2001). (b) DSS image showing the stellar field and $H\alpha$ emission from the $H\ II$ region, with the approximate location of the $\sim 17' \times 17'$ ACIS-I array in our observation outlined in black. (c) JHK image of the central region (roughly $23' \times 25'$) from the 2MASS survey, showing the NGC 6618 stellar cluster and ionized gas surrounded by the dark molecular cloud (Atlas Image courtesy of 2MASS/UMass/IPAC-Caltech/NASA/NSF); again the approximate location of the ACIS-I array is overlaid. (d) *ROSAT* PSPC X-ray image of M17 and vicinity, with the approximate location of the ACIS-I array outlined in blue. In these and all following images, north is up and east to the left unless otherwise noted.

In the visual band, the Digitized Sky Survey (DSS) red image is dominated by $H\alpha$ nebulosity from the northern bar, but emission from the southern bar and ionizing cluster is largely absorbed (Fig. 1b). At low surface brightness, the DSS image shows $H\alpha$ extending over $\sim 20' \times 20'$ with features closely correlated with the low-frequency radio structures where extinction is low; particularly noticeable are a few large arc-shaped features. Optical spectroscopy has shown high-excitation optical emission lines rarely seen in other H II regions (Glushkov 1998). Near-infrared images suffer less obscuration and clearly display line emission from the bars seen in the radio, as well as the exciting stellar cluster (Fig. 1c). Recent deep near-infrared observations reveal a circular cavity in the gas around the exciting cluster as well as many cluster members and embedded young stars in the surrounding dark cloud (Ando et al. 2002; Jiang et al. 2002).

In the X-ray band, M17 was observed with *ROSAT* for 6.7 ks; the findings have just recently been published (Dunne et al. 2003, hereafter Dunne03). We show the *ROSAT* Position Sensitive Proportional Counter (PSPC) “full band” (0.1–2.4 keV) image, slightly smoothed with a Gaussian kernel, in Figure 1d; contours from this exposure are superposed on a new $H\alpha$ image in Dunne03 (their Fig. 1). The X-ray image shows strong emission around the core of the ionizing cluster and an elongated structure extending $20'$ to the east-southeast, parallel to the northern bar and filling the optically thick part of the DSS image. Extended, fainter emission matching the diffuse $H\alpha$ emission is visible toward the east and north; no limb-brightening is seen. Dunne03 found $kT = 0.66\text{--}0.78$ keV ($T = 7.7\text{--}9.1$ MK) and $N_H = (1\text{--}5) \times 10^{20}$ cm $^{-2}$ for this emission, with electron densities of $n_e \sim 0.06\text{--}0.09$ cm $^{-3}$ and a total luminosity (in the 0.1–2.4 keV band) of $L_X \sim 2 \times 10^{33}$ ergs s $^{-1}$. For the area of bright X-ray emission close to the ionizing cluster, the *ROSAT* spectrum was not well-fitted, but Dunne03 estimate $L_X \sim 1 \times 10^{33}$ ergs s $^{-1}$ for this region.

Dunne03 note that the region is too young to have produced a SNR and interpret the X-ray emission as hot gas filling a superbubble blown by the OB star winds, but they note that the *ROSAT* X-ray luminosity for this region is three orders of magnitude lower than the predictions of standard wind-blown bubble models. They conclude that the discrepancy may be due in part to the inclusion of heat conduction across the interface between the hot X-ray-emitting region and the cool swept-up shell in those models, whereas the strong magnetic field in M17 (Brogan & Troland 2001) may suppress this heat conduction. They thus consider a bubble without heat conduction but can only reproduce the observations by assuming substantial mixing of cold nebular gas with the shocked stellar winds; they further require the stellar winds to be clumpy (Moffat & Robert 1994) and to have reduced mass-loss rates in order to get reasonable agreement between the models and their observations.

An observation with the *ASCA* satellite, which has a broad point-spread function (PSF), shows emission coincident with the cluster core with 0.5–10 keV luminosity $L_X \sim 10^{33}\text{--}10^{34}$ ergs s $^{-1}$, with high plasma energy ($kT > 3$ keV, or $T > 35$ MK) and absorption [$N_H = (1\text{--}5) \times 10^{22}$ cm $^{-2}$; Matsuzaki et al. 1999]. These authors interpreted the emission as a point source associated with the single O4-O4 binary system, but we establish here that their spectrum is comprised of emission from many hundreds of cluster members.

On the western side, all tracers of warm and hot gas are truncated by a wall of dense, cold molecular material that includes the dense cores known as M17 Southwest and M17 North; these exhibit many other tracers of current massive star formation. These include the Kleinmann-Wright object, an embedded $L_{\text{bol}} \simeq 2600 L_\odot$ Herbig B2e star; M17-UC1, an extremely small (diameter ~ 1000 AU) and dense ultracompact region powered by a very young massive binary system with a luminosity of several thousand L_\odot ; the even more luminous, but radio-faint, protostar IRS 5; and a deeply embedded millimeter-infrared source (Johnson, Depree, & Goss 1998; Henning et al. 1998; Chini, Nielbock, & Beck 2000; Nielbock et al. 2001; Kassis et al. 2002). There is a strong suspicion that shocks from the blister H II region have compressed the cloud and triggered this star formation activity. The exact structural relationships between the cold and warm gaseous components are not certain; for example, neutral-hydrogen clumps may be mixed with H II gas on the edge of the molecular cloud (Clayton et al. 1985).

Only the most massive members of the young NGC 6618 stellar cluster exciting the nebula have been characterized, because of the comparatively high extinction. Near-infrared imagery and spectroscopy reveal an embedded cluster of about 100 stars earlier than B9 (Lada et al. 1991; Hanson et al. 1997); see Table 5 in Appendix A for a list of O–B3 stars. These studies did not cover the entire cluster, so even more early stars may be present. This is substantially richer than the Orion Nebula cluster (ONC), which has only eight stars between O6 and B9 (Hillenbrand 1997). Hanson et al. (1997) report the age of the cluster, obtained from isochronal fitting, to be ~ 1 Myr or younger. Many of the stars in M17 show infrared excesses attributed to disks, and a considerable fraction are close binaries (García & Mermilliod 2001). The extinction is patchy, ranging from $A_V = 3$ to 15 with an average of 8 mag. From main-sequence fitting of the OB stars, the distance to M17 has been measured to be $1.3^{+0.4}_{-0.2}$ kpc (Hanson et al. 1997) and 1.6 ± 0.3 kpc (Nielbock et al. 2001), significantly closer than the traditional value of $\simeq 2.2$ kpc based on the Galactic rotation curve. We adopt here a distance of 1.6 kpc.

In summary, prior to the present study, M17 was known to have four major morphological components: (1) An inner, bright photoionized nebula with a hollow, conical shape, with gas concentrated in the northern and southern bars. The gas in the bars, photoexcited by the early OB stars, has $T_e \sim 8000$ K and $n_e \sim 10^3$ cm $^{-3}$. (2) An outer, fainter, optically thin ionized region, also with extended soft X-ray emission seen by *ROSAT*, with $T_X \sim 8$ MK and $n_e \sim 0.1$ cm $^{-3}$. This outer region lies largely outside the field of view (FOV) of our *Chandra* observation. (3) Dense, cold molecular gas surrounding the two bars with active star formation, including new rich stellar clusters. (4) The open cluster NGC 6618, which excites the nebula.

2.2. Rosette

The Rosette Nebula [= NGC 2237–2246, at $(l, b) = (206^\circ.4, -2^\circ.0)$] is powered by the open cluster NGC 2244, the youngest cluster within the larger Mon OB2 association. It is a blister H II region lying on the edge of the giant Rosette molecular cloud (RMC), which in turn lies within a larger H I cloud (see Pérez 1991 for a review of the large-scale star formation environment). Because of the orientation with respect to the line of sight, the extinction to the

stars and nebula is lower than for M17, generally only $A_V \sim 1\text{--}2$ mag (Celnik 1986).

The Rosette is morphologically similar to M17 in that the nebular emission is edge-brightened, although in the case of Rosette it resembles a torus (in projection) rather than two bars. At both radio and visual wavelengths (Figs. 2a and 2b), the Rosette H II region appears as a thick circular ring of ionized gas with an outer diameter of $\sim 80'$ (~ 33 pc) and an inner hole of $\sim 30'$ (~ 12 pc) in extent (Celnik 1985). The *IRAS* data show a similar annular morphology extending beyond the H II region into the photodissociation region and surrounding molecular cloud (see Fig. 2c; from Cox, Deharveng, & Leene 1990). Researchers have variously suggested that this annular or “hollow” H II morphology arises from evacuation by the OB stellar winds or by the depletion of gas into newly formed stars (Mathews 1966; Fountain, Gary, & Odell 1979; Leahy 1985; Dorland, Montmerle, & Doom 1986; McCullough 2000). The shape of the nebula is generally considered to be spherical, but it may equally well be cylindrical.

The H II region was modeled by Celnik (1985) to explain the radial distribution of brightness temperature derived from radio continuum observations. In these data, $T_e = 5800$ K and showed no radial gradient. The favored model consists of a central spherical cavity surrounded by nested spherical shells of varying density (maximum $n_e \sim 12$ cm $^{-3}$), with a conical hole penetrating the shells and oriented approximately along the line of sight. This model is further developed by Celnik (1986) into a three-dimensional model of the entire RMC and Rosette Nebula complex. In this model, the H II region is located on the near side of the molecular cloud complex; it and the molecular clouds are rotating about the center of the complex. The conical hole penetrating the shells of the H II region is oriented roughly 30° west of the line of sight, toward the nearest edge of the molecular cloud.

In a recent paper, Tsivilev et al. (2002) describe radio recombination line observations of Rosette, giving $T_e = 7980 \pm 580$ K. They build a model of the region, using a constant, average $T_e = 6400$ K and assuming that the region consists of concentric shells, similar to the Celnik (1985) model. The main new feature of the Tsivilev et al. (2002) model is the inclusion of dense clumps of material in the shells. To match the data, their model required two shells: an outer one with uniform density $n_e = 15$ cm $^{-3}$, similar to the Celnik (1985) model, and an inner one with high-density clumps ($n_e \sim 10^3\text{--}10^4$ cm $^{-3}$).

The RMC, extending a degree to the east (see Fig. 2c), is a clumpy, elongated giant molecular cloud with no evidence for cloud compression or star formation close to the H II region (Williams, Blitz, & Stark 1995). The densest parts of the cloud are populated with embedded near-infrared star clusters without massive ($L_{\text{IR}} \sim 10^3 L_\odot$) members (Phelps & Lada 1997; Schneider et al. 1998), although massive young B stars such as AFGL 961 are also seen in the *IRAS* data (Cox et al. 1990).

The NGC 2244 cluster exciting the nebula has a population intermediate between that of M17 and the ONC, with 31 stars between O4 V and B3 V (Table 6 in Appendix A). It has a core radius of ~ 2 pc ($\sim 4.9'$), an outer radius of ~ 8 pc ($\sim 19.5'$), and low stellar density; thus, it shows substantial contamination from field stars (Nilakshi et al. 2002). Curiously, the earliest exciting star [HD 46223, O4 V((f)); see Table 6] does not lie near the center of the nebula, but

rather near the southeast edge of the ring. The other early O star [HD 46150, O5 V((f))] is located near the center of the nebula. The main-sequence turnoff age of the cluster is about 1.9 Myr (Park & Sung 2002), which agrees with the age inferred from the eclipsing binary V578 Mon (Hensberge, Pavlovski, & Verschueren 2000). This young age, together with the absence of nonthermal radio emission, indicates that no supernova explosion has occurred in the cluster (this point is discussed further in § 6.3). The most accurate distance to NGC 2244, $d = 1.39 \pm 0.1$ kpc, is derived from modeling V578 Mon (Hensberge et al. 2000). We adopt a distance of 1.4 kpc here.

As mentioned above, an *Einstein Observatory* Imaging Proportional Counter observation of NGC 2244 revealed several individual O stars and extended X-ray emission from the nebula interior, with $kT \sim 2$ keV ($T \sim 23$ MK), $n_e \sim 0.02$ cm $^{-3}$, and luminosity $L_X = 6 \times 10^{32}$ ergs s $^{-1}$ in the soft (0.5–3 keV) band (Leahy 1985). Leahy attributes this to diffuse emission from the OB winds, but the low resolution provided by this instrument could not determine the fraction of the emission from the many magnetically active lower mass pre-main-sequence stars expected to accompany the massive stars. Indeed, a later higher resolution *ROSAT* study by Berghöfer & Christian (2002; see Fig. 2d) attributed all of the emission to point sources. This *ROSAT* study (see also the closely related work of Li et al. 2002 and Park & Sung 2002) identified 128 X-ray-emitting pre-main-sequence stars in addition to 10 OB stars. A separate *ROSAT* observation of the RMC revealed dozens of faint, partially resolved embedded sources attributed to individual Herbig Ae/Be stars and clusters of low-mass pre-main-sequence stars (Gregorio-Hetem et al. 1998).⁵

One aspect of the Rosette star formation region is still unclear: Was the formation of the cluster triggered by an encounter between the large Monoceros Loop SNR, seen in radio continuum and H α , and the RMC? The SNR may have been produced by a massive member of the Mon OB2 association; it has a diameter of ~ 80 pc and is centered 2° to the northeast of the Rosette Nebula. Older studies placed it at about the same distance as NGC 2264 (~ 800 pc), but more recent estimates from a CO survey of the Mon OB1 region (Oliver, Masheded, & Thaddeus 1996) suggest that it lies at approximately the same distance as the NGC 2244 stellar cluster; note, however, that it has an estimated age of only 0.03–0.5 Myr (Welsh et al. 2001). Given a cluster age of 1.9 Myr (see above), the evidence suggests that the cluster formed earlier than any possible encounter with the SNR. Extended high-energy γ -ray emission has been found by the EGRET instrument around the region of apparent contact between the SNR and the nebula, interpreted in terms of π^0 decay resulting from collisions between SNR-accelerated particles and the molecular cloud (Jaffe et al. 1997). However, no morphological indication of a collision or compression is evident from optical or molecular maps.

In summary, and by analogy with M17, the major morphological components of the Rosette star formation

⁵ This study noted strong X-ray emission at the edge of the *ROSAT* PSPC field toward the H II region and speculated that it arose from either unresolved emission from T Tauri stars or from OB wind emission. It is now clear that this is emission from the unresolved O4 V star HD 46223 blurred by the poor PSF at that off-axis location in the *ROSAT* image.

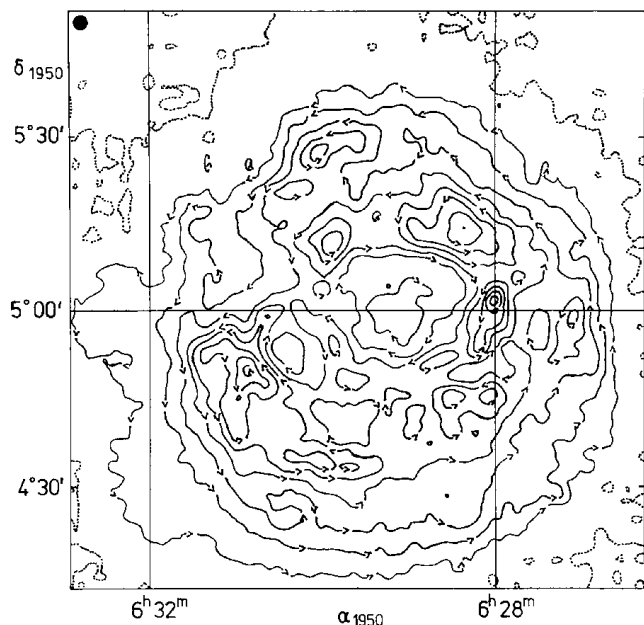


FIG. 2a

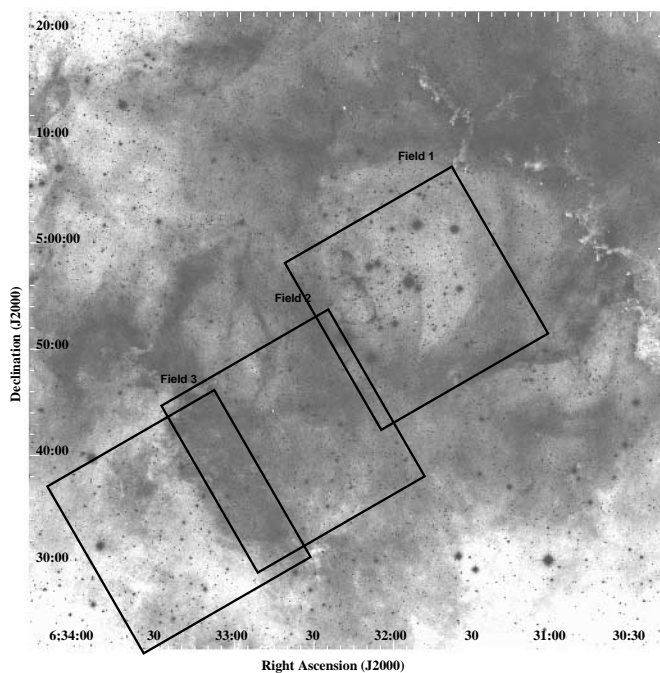


FIG. 2b

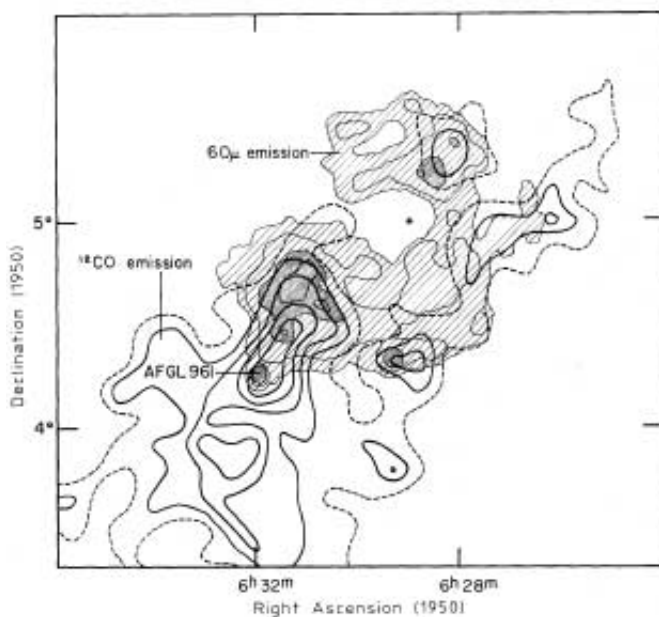


FIG. 2c

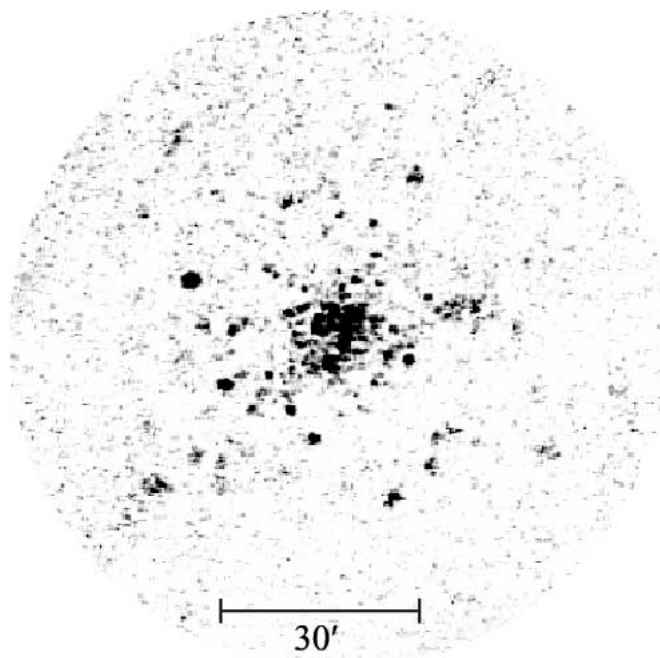


FIG. 2d

FIG. 2.—Multiwavelength views of the Rosette Nebula and RMC. (a) Radio continuum map showing H II gas, from Celnik (1985). (b) DSS image of the Rosette Nebula with overlays showing the approximate locations of the first three ACIS-I fields. (c) Contour map of molecular CO in the RMC with $60\ \mu\text{m}$ IRAS emission superposed and the central cluster marked by an asterisk, from Cox et al. (1990). (d) ROSAT PSPC X-ray image of the open cluster NGC 2244, from Berghöfer & Christian (2002).

region are (1) An edge-brightened, photoionized nebula with a hollow, spherical (or cylindrical) shape, perhaps with a conical cavity expanding toward the nearest edge of the surrounding molecular cloud. The central region showed extended X-ray emission with *Einstein*, with $T_X \sim 23\ \text{MK}$ and $n_e \sim 0.02\ \text{cm}^{-3}$, but *ROSAT* studies resolved this emission into point sources. Shells of higher density surround the hollow core, with $T_e \sim 6400\ \text{K}$, per-

haps a clumpy inner shell with $n_e \sim 10^3\text{--}10^4\ \text{cm}^{-3}$, and an outer shell or shells with $n_e \sim 10\ \text{cm}^{-3}$ (Celnik 1985; Tsvilev et al. 2002). (2) A photodissociation region between the Rosette blister H II region and its molecular cloud. (3) Dense, cold molecular gas making up the RMC and extending far beyond the H II region, where new stellar clusters are forming. (4) The open cluster NGC 2244, which excites the nebula.

3. CHANDRA OBSERVATIONS AND ANALYSIS

The H II regions were observed with the Imaging Array of *Chandra*'s Advanced CCD Imaging Spectrometer (ACIS-I); the observatory and instrument are described by Weisskopf et al. (2002). CCDs S2 and S3 from the Spectroscopy Array were also operating, although these chips are more than 15' off-axis and not positioned to match the ACIS-I focal surface, so they exhibit large, distorted PSFs that make point-source detection difficult. They are nonetheless useful for broad characterization of diffuse emission and for revealing the presence of bright point sources. The observing mode was the standard "Timed Event, Faint" mode, with 3.2 s integration times, 0.041 s frame readout times, and 3 pixel \times 3 pixel event islands.

Table 1 gives the observing log. M17 was observed in a single 39 ks pointing centered on the heavily obscured O4-O4 binary known as Kleinmann's Anonymous Star in the NGC 6618 cluster (star No. 1 in Chini, Elsässer, & Neckel 1980, No. 341 in Ogura & Ishida 1981, and No. 189 in Hanson et al. 1997). The Rosette observation consisted of a contiguous sequence of four \sim 20 ks ACIS-I snapshots (Fields 1–4), resulting in a \sim 1° \times 0°:25 mosaic of the Rosette Nebula and RMC. The aim point of Rosette Field 1 was placed near the center of the Rosette Nebula on the B star HD 259105, to avoid photon pileup of the O5 star HD 46150. An unfortunate telescope roll angle about this aim point led to HD 46150 falling in the gap between CCDs I2 and I3, resulting in substantially reduced exposure for this important early O star. Rosette Field 2 yields the best image of the interface between ionized material in the H II region and neutral material in the RMC. Fields 3 and 4 step eastward into the molecular cloud, sampling the young, embedded stellar population there.

Our custom processing, starting with the Level 1 data stream, is described in Appendix B. Important steps include removal of the 0".5 position randomization and correction of the CCD charge transfer inefficiency (CTI) to improve spectral resolution (Townesley et al. 2002b). We generated custom response matrix files (RMFs) and quantum efficiency uniformity files (QEUs) to facilitate spectral fitting of CTI-corrected data (Townesley et al. 2002a).⁶ The images are registered with the USNO-A2.0 catalog⁷ or *Hipparcos* sources (Høg et al. 2000) in the field to improve the astrometry; this alignment is accurate to about \pm 0".3.

⁶ Details, source code, and calibration products for CTI correction using our method are available at <http://www.astro.psu.edu/users/townsley/cti>.

⁷ See D. B. A. Monet et al. (1998), VizieR Online Data Catalog, 1252.

To search for and quantify any diffuse emission in the regions, we have performed a variety of smoothing and image-processing steps; the results are shown in Figures 3–5 for M17 and Figures 6 and 7 for Rosette. For display purposes, the photon-counting images are smoothed with an adaptive kernel filter using the *csmooth* program (a translation of the *asmooth* code by H. Ebeling), part of the CIAO data analysis system supplied by the *Chandra* X-Ray Center (CXC). The ACIS-I exposure maps, which take into account a variety of effects (e.g., bad CCD columns, gaps between the CCDs, telescope vignetting, and satellite dithering), are similarly smoothed, and the resulting photon and exposure images are divided to give a view of the X-ray flux distribution with all known instrumental effects removed.

Figures 3a and 6a show the ACIS-I flux images at this stage of the data processing. The images here are shown at reduced resolution after adaptive kernel smoothing with *csmooth*. In these two-color images, red intensity is scaled to the soft (0.5–2 keV) brightness, and blue intensity is scaled to the hard (2–8 keV) brightness. For clarity, the soft and hard smoothed images are shown separately in Figures 3b–3c and 6b–6c. Both fields show clear indications of soft extended emission in addition to hundreds of unresolved sources.

Quantitative study of the extended emission requires removal of the point-source events. Point sources were found using the wavelet-based source detection program *wavdetect* (Freeman et al. 2002). After experimentation with the source significance threshold in *wavdetect*, we chose a threshold level $P = 1 \times 10^{-5}$. While this results in a number of faint (3–5 counts) and possibly spurious sources, it is more sensitive to clearly real sources that are missed (especially when there is underlying diffuse emission) at the usual threshold of $P = 1 \times 10^{-6}$. The fields were carefully examined by eye to identify potential point sources missed by *wavdetect* because of crowding, diffuse emission, or unknown reasons. The resulting lists of point sources and identifications with members of the NGC 6618, NGC 2244, and RMC stellar clusters will be discussed in separate studies.

Once this liberal list of potential point sources was established for each field, we used our custom IDL code *acis_extract* to excise them from the data.⁸ This tool uses the PSF library in the CIAO Calibration Database to

⁸ The *acis_extract* code is available at http://www.astro.psu.edu/xray/docs/TARA/ae_users_guide.html.

TABLE 1
LOG OF *Chandra* OBSERVATIONS

Target	Date	R.A. (J2000.0)	Decl. (J2000.0)	Integration (s)
M17	2002 Mar 2	18 20 30.39	−16 10 29.7	39440
Rosette Field 1	2001 Jan 5	06 31 52.85	+04 55 42.0	19700
Rosette Field 2	2001 Jan 5	06 32 40.84	+04 42 45.0	19500
Rosette Field 3	2001 Jan 5	06 33 17.15	+04 34 42.0	19410
Rosette Field 4	2001 Jan 6	06 34 17.34	+04 27 45.9	19510

NOTES.—Units of right ascension are hours, minutes, and seconds, and units of declination are degrees, arcminutes, and arcseconds. Positions are for the ACIS Imaging Array aim point. The exposure time is the net usable time after various filtering steps are applied in the data reduction process.

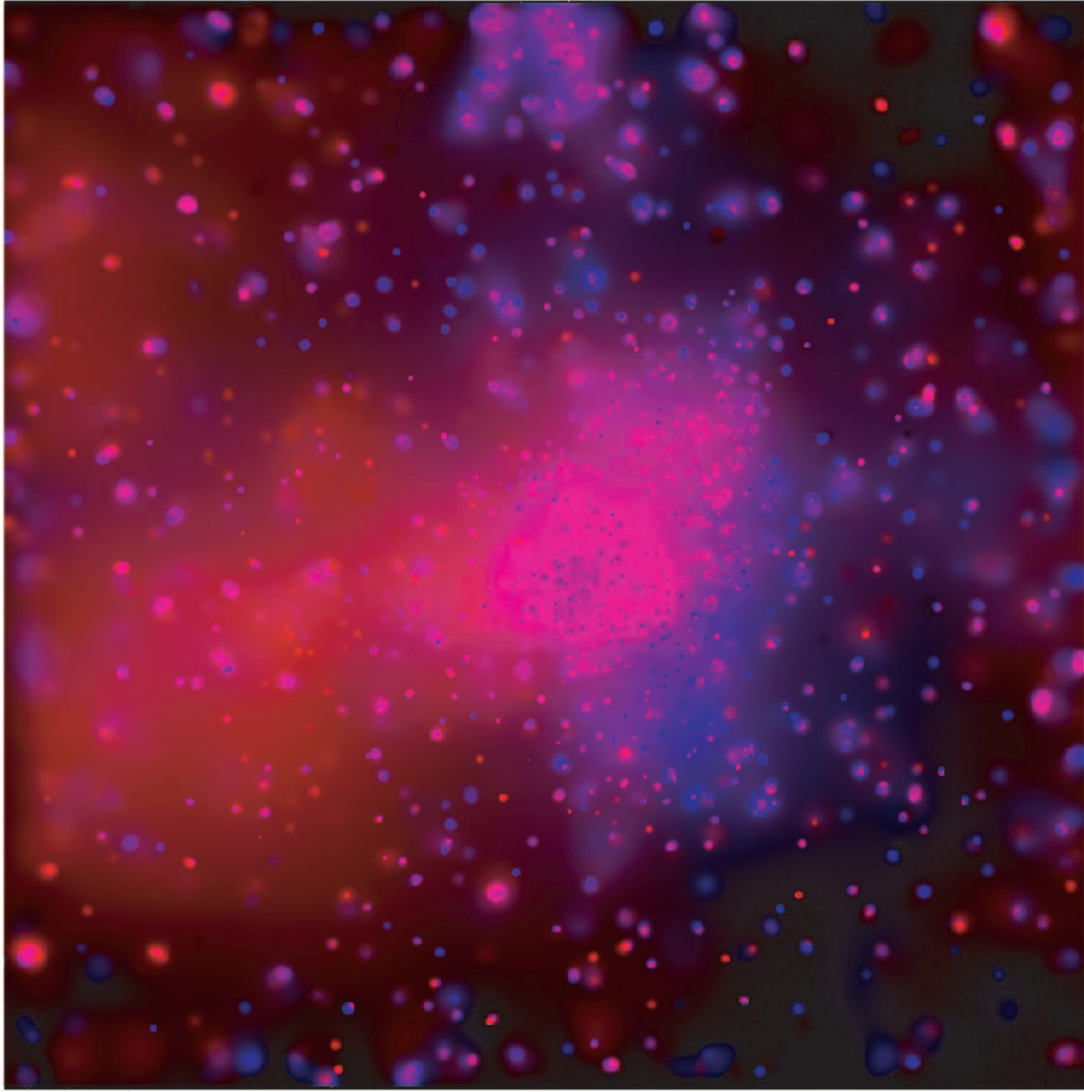


FIG. 3a

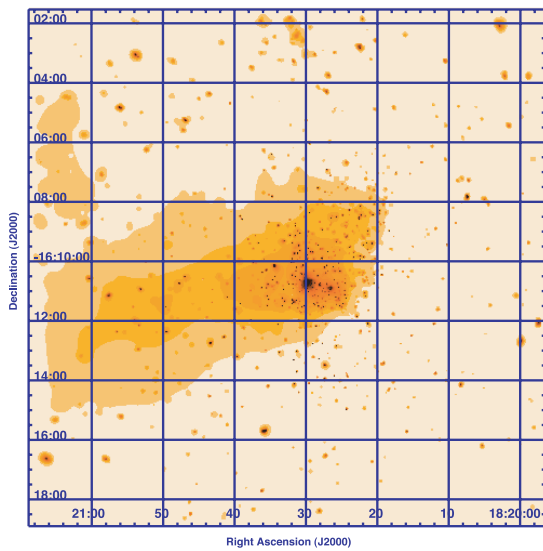


FIG. 3b

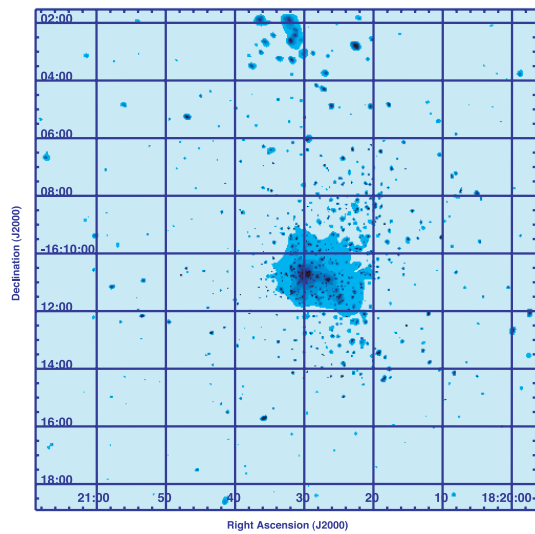


FIG. 3c

FIG. 3.—(a) *Chandra* ACIS-I image of M17 with *csmooth* adaptive smoothing and exposure correction ($2.07 \text{ pixels bin}^{-1}$). Red intensity is scaled to the soft ($0.5\text{--}2 \text{ keV}$) emission, and blue intensity is scaled to the hard ($2\text{--}8 \text{ keV}$) emission. (b) Smoothed $0.5\text{--}2 \text{ keV}$ image used for the red intensity in (a), highlighting the soft diffuse emission. (c) Smoothed $2\text{--}8 \text{ keV}$ image used for the blue intensity in (a), highlighting the hard emission.

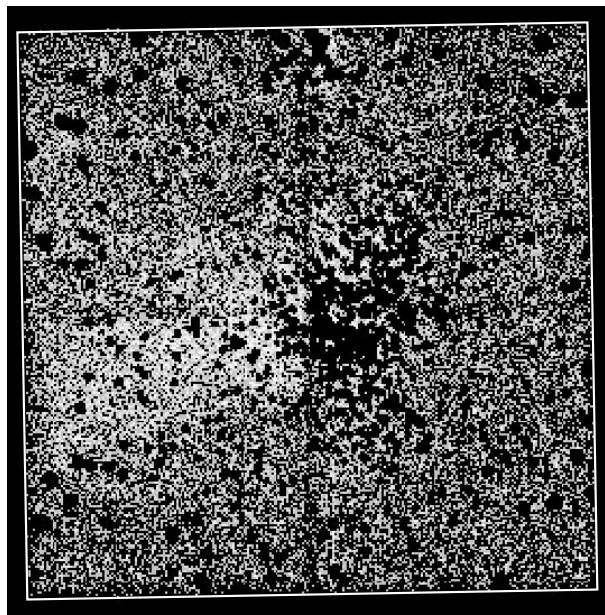


FIG. 4a

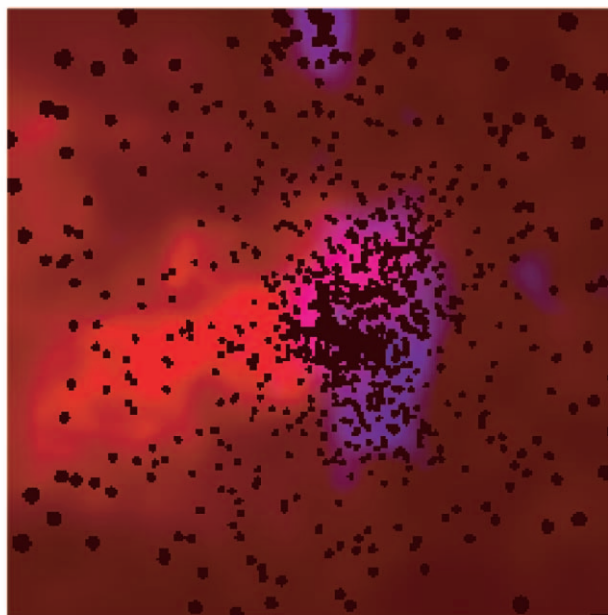


FIG. 4b

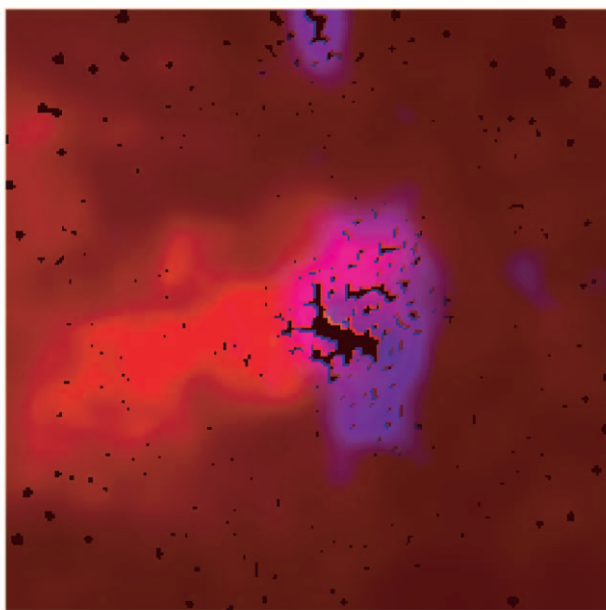


FIG. 4c

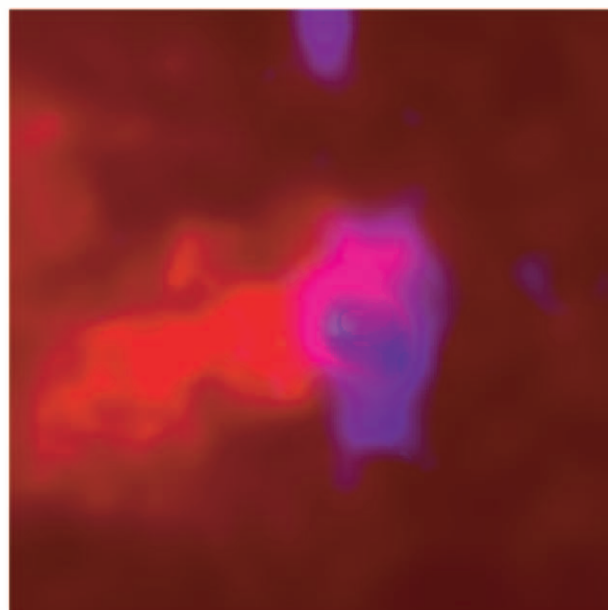


FIG. 4d

FIG. 4.—(a) *Chandra* ACIS-I binned image ($8 \text{ pixels} \times 8 \text{ pixels}$) of M17, 0.5–7 keV, with the more than 900 detected point sources removed for the study of diffuse emission. See § 3 for details. The gaps between the four CCDs in the ACIS-I array are faintly visible. (b) *Chandra* ACIS-I swiss-cheese (sources-removed) image of M17 using our own adaptive smoothing algorithm and exposure correction ($8 \text{ pixels bin}^{-1}$). Red intensity is scaled to the soft (0.5–2 keV) emission, and blue intensity is scaled to the hard (2–7 keV) emission. (c) Same data sets as in (b), with the holes partially smoothed over. (d) Same data sets as in (b), with the holes completely smoothed over. The three smoothed images use identical intensity scaling.

generate a polygon around each source that represents the 99% contour of the PSF at a chosen energy (typically 1.5 keV). A circular exclusion zone is generated with diameter 1.1 times larger than the largest polygon chord. All events within these exclusion zones are deleted, resulting in the “sources-removed” (or, more informally, “swiss-cheese”) event list. The full-band swiss-cheese images for the M17 and Rosette data are shown at reduced resolution (8 pixel binning) in Figures 4a and 7a, respectively.

4. MORPHOLOGY OF THE DIFFUSE X-RAY EMISSION

4.1. M17

Figure 4b shows the $17' \times 17'$ ACIS image of the densest parts of M17, with the ~ 900 sources removed by the swiss-cheese procedure explained above, smoothed with our own adaptive smoothing algorithm. This algorithm understands the absence of data (the holes where point sources were) and

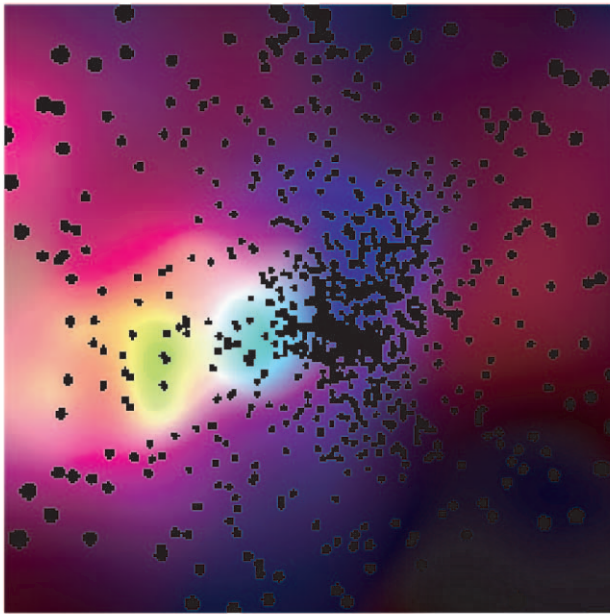


FIG. 5a

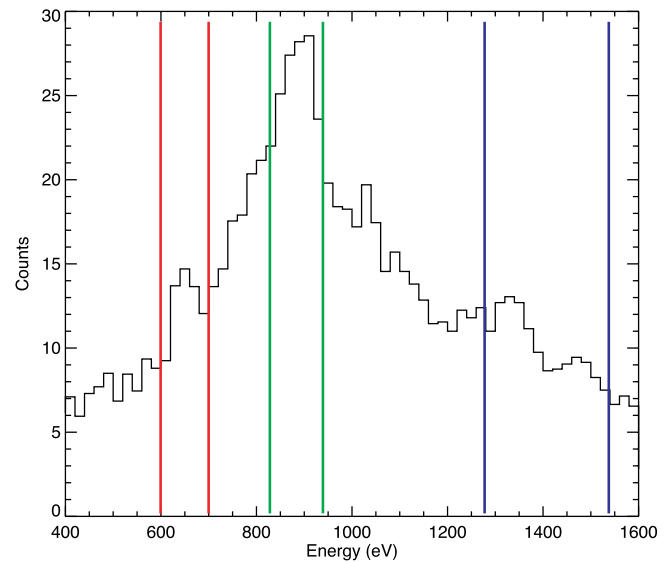


FIG. 5b

FIG. 5.—(a) Three-color image of the smoothed soft diffuse emission in M17. Red: 600–700 eV (1267 events). Green: 830–940 eV (2871 events). Blue: 1280–1540 eV (2623 events). (b) Spectrum of the soft diffuse emission, binned at a constant 20 eV per bin to show the peaks in the emission that were used to define the three soft bands for (a). Vertical bars delineate the bands.

does not introduce edge effects into the smoothed image; see Appendix C for details. Red areas highlight soft (0.5–2 keV) emission, and blue areas highlight hard (2–7 keV) emission.⁹ The holes from the masked point sources are shown at their full size in Figure 4b to give a smoothed representation of the data that still retains much of the character of the simple binned image (Fig. 4a). Figure 4c shows these holes partially smoothed over; in Figure 4d they are completely smoothed over. These three versions of the adaptively smoothed unresolved emission in M17 are shown to provide the reader with an incremental transition from the swiss-cheese image to the fully smoothed image; the intent is to illustrate that, although smoothing can reveal morphological features impossible to see in the binned data, it can cause the viewer to lose track of the actual amount of information that went into the smoothed image. These smoothed images are reassuringly similar to the *csmooth* image in Figure 3a.

Figure 5 explores the soft diffuse emission in more detail. Figure 5a shows a three-color image of the soft emission with the point-source masks in place; here red = 600–700 eV, green = 830–940 eV, and blue = 1280–1540 eV. The spectrum in Figure 5b uses 20 eV bins to show the line features that motivated the bands selected for Figure 5a. The three-color image allows us to scale the brightness of the 600–700 eV component up to show faint soft features; a slight enhancement to the northwest of the core of NGC 6618 is visible in this image. This image hints at a possible softening of the X-rays with distance away from the ionizing cluster; although our spectral analysis to search for changes

in the temperature of the gas as a function of distance from the ionizing cluster showed no such evolution (see § 5.2), the wider region sampled by *ROSAT* shows a slight spectral softening to the north, consistent with Figure 5a (Dunne03).

The smoothed images in Figures 3 and 4 are clearly closely related to the Two Micron All Sky Survey (2MASS) near-infrared image (Fig. 1c): the bright soft X-ray contours closely follow the hollow structure of the photoionized region between the northern and southern bars (while fainter emission is spread over a larger area). The brightest soft X-ray emission coincides with the hole in the diffuse H II emission in the deep near-infrared image of Ando et al. (2002) immediately around the exciting stars of the nebula. The hard emission coincides with the central region and crosses the dark region to the west of the steep interface between the photoionized bars and the molecular cloud. Another patch of hard emission is associated with the deeply embedded M17 North region. As discussed below, the most likely source of this very slight excess of hard photons is the unresolved point source population in these embedded star-forming regions. The smoothing algorithm enhances the appearance of this emission, but its proximity to regions of large point-source concentrations makes this the simplest explanation.

The overall morphology of the soft diffuse emission in the ACIS image of M17 strongly suggests that the hot gas originates in the OB cluster and flows outward toward the lower density regions to the east. This might be called an “X-ray fountain,” representing the flow of shocked OB winds into the hot interstellar medium. The *ROSAT* PSPC image confirms this view: in the optically thick inner H II region, its contours are elongated identically to the ACIS emission, while in the outer regions, it reveals the X-ray flow extending several parsecs to the east and north; this is illustrated

⁹ For all smoothed swiss-cheese images of diffuse emission, we clipped the hard band at 7 keV to avoid contamination from the faint instrumental Ni K α line at 7.47 keV.

clearly in Dunne03 (their Fig. 1). Since 10^4 K H II region gas and 10^7 K X-ray gas cannot stably coexist in the same volume, it is likely that the X-ray gas fills the interior of the cylindrical or conical inner region defined by the radio/optical H II bars.

Farther to the east, the X-ray gas expands into the lower density, optically thin region, filling a cavity in the DSS image. We suspect that the X-ray-filled cavity extends farther to the north and east as traced by 330 MHz radio emission but is obscured in both soft X-rays and H α by intervening cloud material. The X-ray-emitting area may thus be 2–3 times larger than seen with *ROSAT* and several times larger than seen in our single $17' \times 17'$ *Chandra* pointing.

In summary, the soft X-ray images of M17 from *ROSAT* and *Chandra*, combined with radio, optical, and near-IR data, strongly suggest a dynamic rather than static hot plasma, generated at the OB star cluster and flowing into (and perhaps even creating) the low-density, blister-like cavity extending 5–10 pc away from the molecular cloud. It is then unclear whether the features in the H α maps—wisps, arcs, and filaments—are manifestations of OB photoionization or direct thermal contact with the hot, X-ray-emitting gas.

4.2. Rosette

Figure 7*b* shows the full ACIS image of the Rosette Nebula, with the ~ 350 sources removed by the swiss-cheese procedure explained above and again smoothed with our own adaptive smoothing algorithm (see Appendix C). Red areas highlight soft (0.5–2 keV) emission, and blue areas highlight hard (2–7 keV) emission. The holes from the masked point sources are shown at their full size in Figure 7*b*; Figure 7*c* shows these holes partially smoothed over, and in Figure 7*d* they are completely smoothed over. Again, these images are similar to the *csmooth* versions in Figure 6. The brightest areas of diffuse emission are coincident with the two early O stars in the field; this is not obvious in the adaptively smoothed images because they have been scaled to highlight faint diffuse emission. The “hot spot” to the southwest of the main region of diffuse emission in Figures 7*b*–7*d* may be due to a point source that was too faint to be detected so far off-axis.

The adaptively smoothed images in Figure 7*b*–7*d* retain the off-axis CCDs S2 (*top left*) and S3 (*top right*). S3 is a backside-illuminated CCD and shows higher background; thus, the apparent high intensity of soft emission is dominated by detector effects, and little useful information on the true soft diffuse emission is available from this device. The S2 chip may be affected by unresolved point source emission, although the diffuse emission seen in the smoothed images could be real; its spectrum is similar to the soft diffuse emission seen on the ACIS-I CCDs in this pointing.

The diffuse emission found in our *Chandra* mosaic of the Rosette region comes mainly from Field 1, which includes the NGC 2244 exciting cluster, and to a lesser extent from the northwest part of the adjacent Field 2 (see Fig. 6*b*). Diffuse emission may very well extend outside of our ACIS fields. The total number of diffuse photons in our ACIS images of Rosette is 3 times smaller than in our M17 image; thus, the spectral and morphological information is limited. A longer *Chandra* exposure of Field 1 is approved for more detailed study.

With these limitations in mind, the morphology of the Rosette diffuse X-ray emission shown in the adaptively smoothed images in Figure 6 and 7 is similar to that in M17. It appears centrally brightened, centered to the southeast of the axis of the ionized H II torus toward the two earliest stars of the exciting cluster, HD 46223 and HD 46150 (see Table 6 in Appendix A). The surface brightness is highest around these two early O stars and decreases outward, with possible leakage beyond the edge of the ionized shell toward the southeast, where there is a suggestion of a cavity in the optical H II region (Fig. 2*b*). In light of the M17 morphology described in § 4.1, we can speculate that the Rosette Nebula diffuse emission might also be an X-ray fountain generated by the exciting cluster NGC 2244 but seen almost along, rather than perpendicular to, the outflow axis, perhaps flowing out through the conical cavity proposed by Celnik (1986). The fact that the Rosette diffuse emission is substantially weaker than that in M17 is consistent with production by OB stellar winds, which are fewer and weaker in Rosette (compare Tables 5 and 6).

5. QUANTITATIVE STUDY OF THE EXTENDED EMISSION

5.1. Spectral Analysis Methodology

The ACIS detector gives moderate-resolution X-ray spectra for each of roughly 100,000 independent spatially resolved locations across its $17' \times 17'$ FOV. Having spatially decomposed the images into pixels containing point-source photons and pixels containing diffuse-source photons (§ 3), we can readily construct composite spectra for these components. For M17, we selected the part of the ACIS-I image that contained the brightest diffuse emission (called “Total Diffuse Region” in Fig. 8*a*) and extracted the diffuse-emission spectrum from only that region; for Rosette, we extracted counts from the entire ACIS-I array to form the diffuse-emission spectrum. For both fields, composite point source spectra were extracted by using all the point sources in the ACIS-I array.

The background contribution should be small for the point-source components, since the source events were extracted from regions tailored to contain only the inner 90% of each source’s PSF. Background removal for the faint diffuse components, however, must be performed carefully. For the Rosette diffuse emission fit, we subtracted a background spectrum obtained from the S2 chip, which lay outside the core of the cluster.¹⁰ This background spectrum was scaled by the effective area (BACKSCAL was converted to an energy-dependent vector) and by the ratio of the geometric areas. Further scal-

¹⁰ We chose to form the Rosette Field 1 background from the off-axis S2 data, rather than using the I-array data from one of the other Rosette fields, because there was a background flare during the Field 1 observation. This flare was of modest brightness but lasted for 30% of the 20 ks observation. The hard (2–8 keV) band emission varied erratically up to a factor of 3 higher than the usual background level. The variations were much less evident in the soft (0.5–2 keV) band, rising less than 50% in the 1–2 keV range and negligibly below 1 keV. Since flares clearly affect the spectral shape of the background, we determined that better background subtraction could be achieved by using the off-axis S2 data (with appropriate scaling) rather than a different observation. Our composite point source spectral analysis for Rosette Field 1 was restricted to the 0.7–5 keV band to minimize the effect of these background variations.

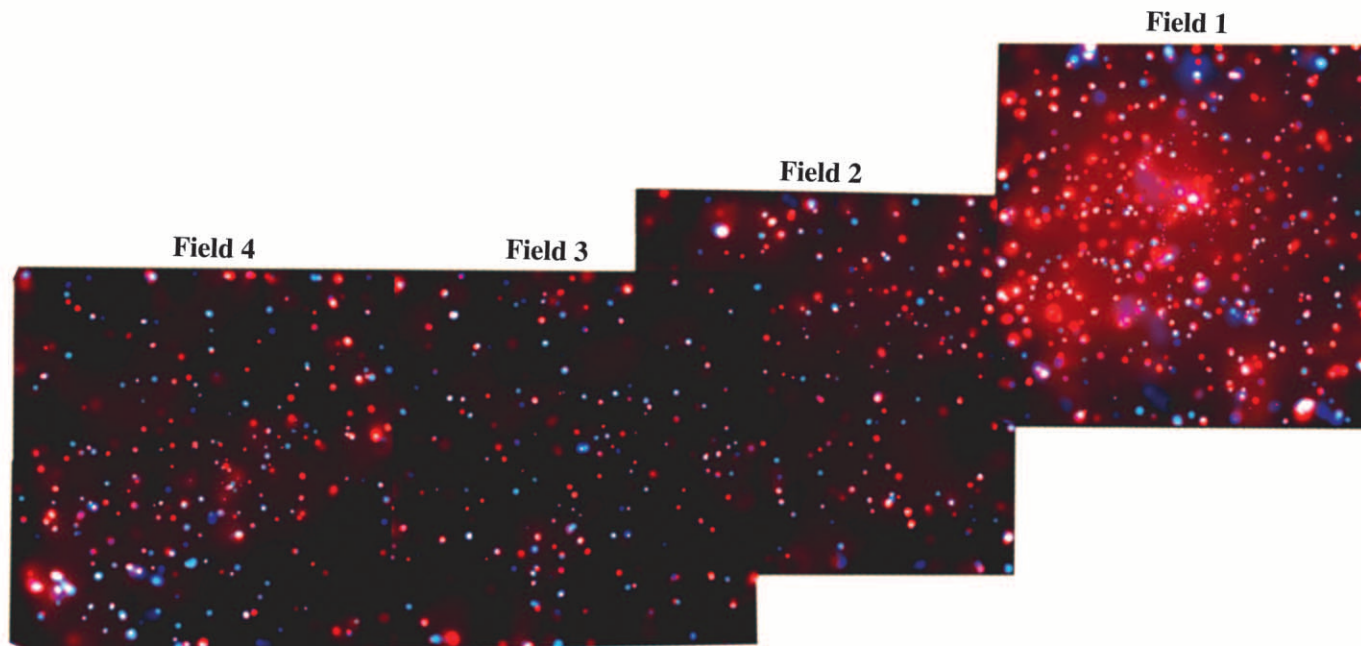


FIG. 6a

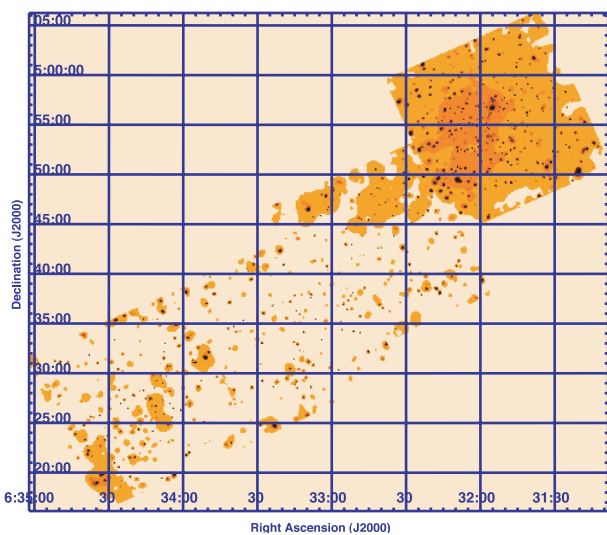


FIG. 6b

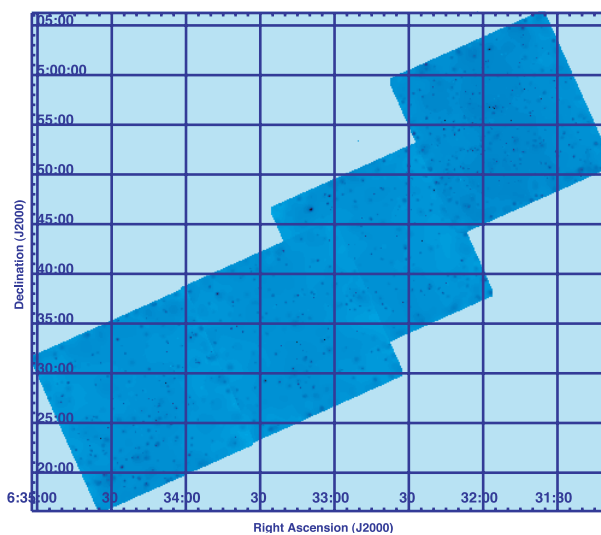


FIG. 6c

FIG. 6.—(a) *Chandra* ACIS-I $1^\circ \times 0^\circ 25'$ mosaic of the Rosette Nebula and RMC, after *csmooth* adaptive smoothing and exposure correction ($2.65 \text{ pixels bin}^{-1}$). Red intensity is scaled to the soft (0.5–2 keV) emission, and blue intensity is scaled to the hard (2–8 keV) emission. This image has been rotated to fit better on the page; the actual orientation of the field on the sky is given in the bottom panels. (b) Smoothed 0.5–2 keV image used for the red intensity in (a), highlighting the soft diffuse emission. (c) Smoothed 2–8 keV image used for the blue intensity in (a), showing that there is no significant hard diffuse emission in this field.

ing was done to account for the nonuniform spatial distribution of the particle background,¹¹ obtained by matching the strength of the instrumental Ni $K\alpha$ line and the 3–7 keV continuum level. The prominent Au M line complex (around 2.1 keV) remaining in the spectrum after background subtraction (see Table 3 in Townsley et al. 2002a) may indicate that the spatial distribution of

Au M fluorescent photons (which come from bombardment of gold-coated surfaces of the ACIS camera and the telescope by solar energetic particles) does not follow that of the particle background.

Accounting for differences in geometric area, ancillary response files (ARFs), and particle background as described above, and assuming that all emission on S2 is due to background and not unresolved stars or diffuse emission, we estimate that the background accounts for about 58% of the events in our sample of the Rosette diffuse emission. Subtracting this leaves only 3300 source counts distributed

¹¹ C. Grant 2002, private communication; also see <http://space.mit.edu/~cgrant/cti/cti120.html>.

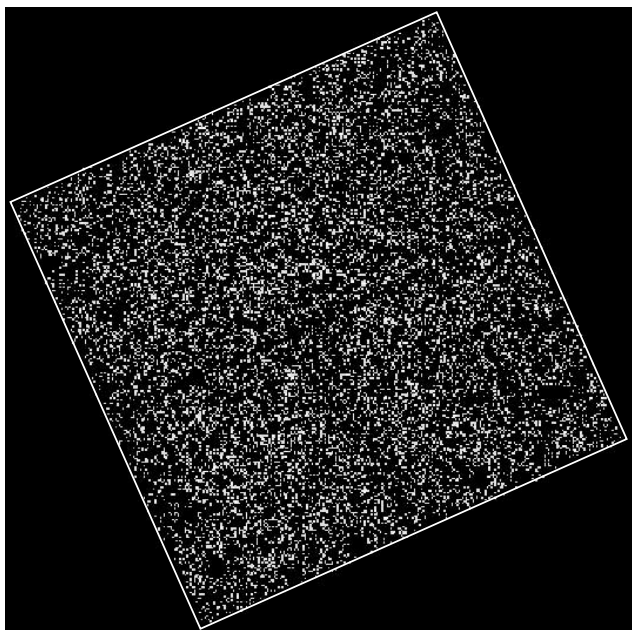


FIG. 7a

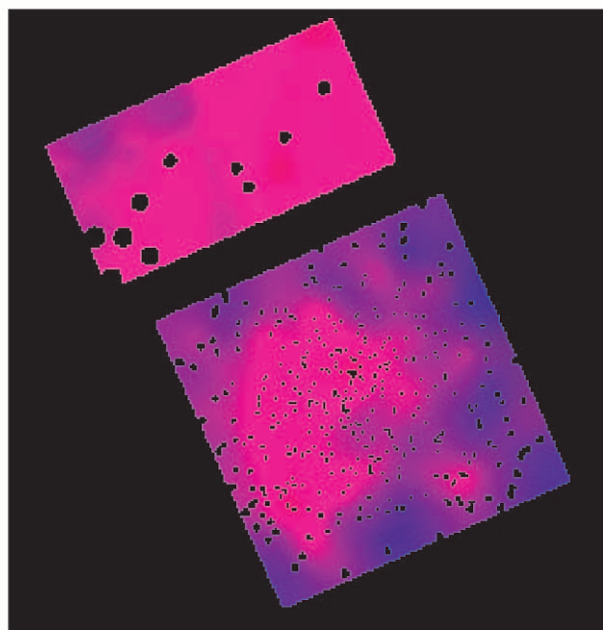


FIG. 7b

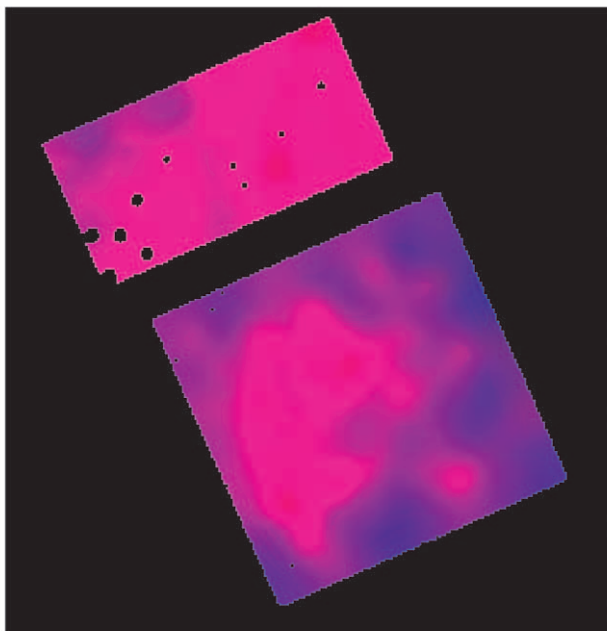


FIG. 7c

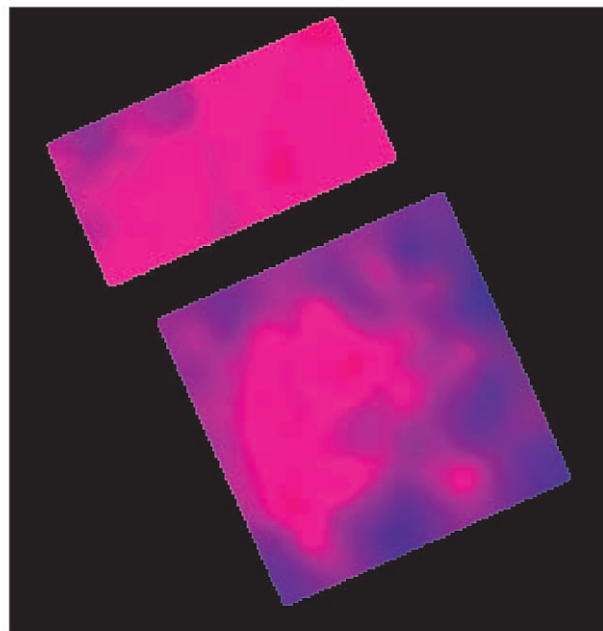


FIG. 7d

FIG. 7.—(a) *Chandra* ACIS-I binned image ($8 \text{ pixels} \times 8 \text{ pixels}$) of the Rosette Nebula pointing (Field 1, the westernmost of the four pointings in the mosaic in Fig. 6a), $0.5\text{--}7 \text{ keV}$, with the more than 350 detected point sources removed for the study of diffuse emission. See § 3 for details. The gaps between the four CCDs in the ACIS-I array are faintly visible. (b) *Chandra* ACIS swiss-cheese (sources-removed) image of Rosette using our own adaptive smoothing algorithm and exposure correction ($8 \text{ pixels bin}^{-1}$). Red intensity is scaled to the soft ($0.5\text{--}2 \text{ keV}$) emission, and blue intensity is scaled to the hard ($2\text{--}7 \text{ keV}$) emission. The off-axis S2 and S3 chips are included at the top of this image; the background on S3 (a BI CCD, top right in the image) is higher than the other CCDs, so no information on diffuse emission there can be inferred from this image. (c) Same data sets as in (b), with the holes partially smoothed over. (d) Same data sets as in (b), with the holes completely smoothed over. The three smoothed images use identical intensity scaling.

over the entire ACIS-I array. Figures 7b–7d imply, however, that some of the S2 photons are not from the background; if this is the case, then our background subtraction removes legitimate photons from the Rosette diffuse emission spectrum, and a smaller percentage of unresolved events come from the background.

For M17, a background region near the southern edge of the I-array around the molecular cloud was used. This background spectrum was also scaled by the effective area and by the ratio of the geometric areas. Scaling the number of $0.5\text{--}2.3 \text{ keV}$ counts in the M17 background area (lower part of I1 chip) to account for the difference

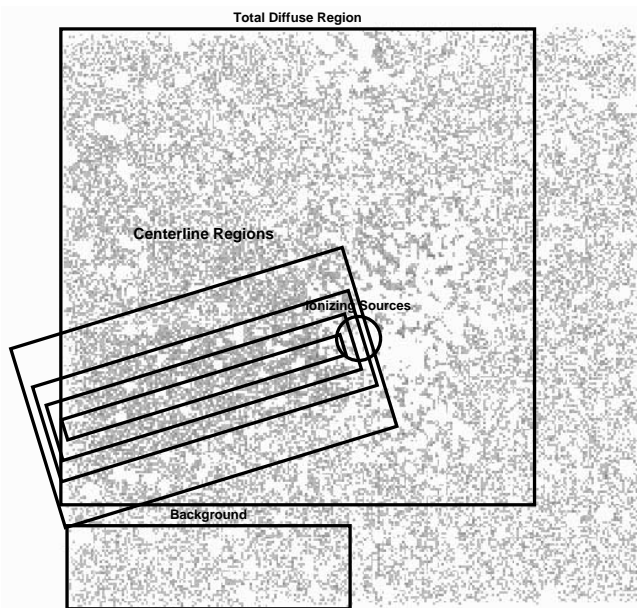


FIG. 8a

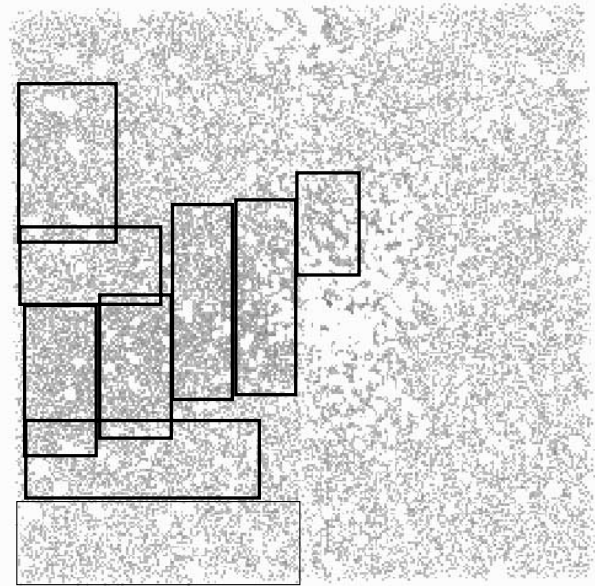


FIG. 8b

FIG. 8.—Regions used for spectral fitting of diffuse emission in M17, overlaid on a full-band, binned, sources-removed image of the diffuse emission. (a) Outlined are the large region used for our spectral analysis of the diffuse emission seen in M17, the region at the bottom of the I1 CCD used as background for that spectral fitting, and the rectangular annuli following the center line of the soft diffuse emission, used to search for temperature gradients away from the center line. The circle represents the approximate location of the ring of O stars at the center of NGC 6618. (b) Other regions used to look for temperature variations in the diffuse emission, particularly as a function of distance from the ionizing O stars. The I1 background region is again shown in light outline at the bottom left.

in geometric area between the diffuse-emission region and the background region, and ignoring any additional scaling due to ARF differences (the exposure map shows that this is a small factor), we find that the background accounts for almost 50% of the events in the diffuse region. This presumes that the region we used for background is free of diffuse emission, but the *ROSAT* image shows that there is faint diffuse emission in this region. The spectrum of this region also resembles that of the diffuse emission. This shows that again our background subtraction is almost certainly removing useful diffuse photons and that the actual background contribution to the diffuse emission is likely less than 50%.

For both Rosette and M17, the regions used to sample the background spectrum are not ideal. We chose not to use generic background files supplied by the CXC because our fields are in the Galactic plane, which is known to contain diffuse X-ray emission from a variety of known (e.g., the Local Hot Bubble; Snowden et al. 1998) and unknown (e.g., the Galactic ridge X-ray emission; Ebisawa et al. 2001) sources. Other nearby regions (Fields 2–4 in the Rosette observation and the western side of the M17 observation, which includes the S2 and S3 chips) sample more obscured parts of the molecular clouds, so backgrounds generated from these regions would not be representative of the regions used to sample the diffuse emission. Thus, rather than choosing background regions that were clearly incorrect, we decided to sample more representative regions and suffer the loss of useful photons.

The background-subtracted diffuse emission spectra, the composite point source spectra, and their associated best-fit plasma models are shown in Figure 9, with details given in Table 2. The spectral fits were performed with XSPEC (Arnaud 1996) using both the *mekal* and *vmekal* thermal

plasma models (Mewe, Lemen, & van den Oord 1986; Kaastra 1992; Liedahl, Osterheld, & Goldstein 1995) and the *apec* and *vapex* models (Smith et al. 2001), where the “v” designation provides for nonsolar abundances of the elements. The fits from both types of models were similar, so only the *apec* class of models is presented here. One or two absorption components were included via the *wabs* model (Morrison & McCammon 1983). An additional absorption component, due presumably to hydrocarbon deposition on the ACIS optical blocking filters (Chartas et al. 2002), was also included in the XSPEC model.¹² The spectral fits employed count-weighted ARFs made using the CIAO utility *mkwarf*. We chose to use the single CTI-corrected RMF (Townsend et al. 2002a) that coincided with the largest fraction of counts. For the full-field spectral fits shown in Figure 9, the RMFs used were the full-CCD versions, so the spectral resolution is the average across the entire CCD after CTI correction (see Appendix B). These full-CCD CTI-corrected RMFs are similar to each other, so using a single-CCD RMF for the entire I-array does not introduce substantial errors.

Table 2 shows that the background-subtracted diffuse emission in both H II regions is reasonably well represented by a two-temperature thermal plasma with a single absorbing column. The temperatures of both plasma components are comparable between the two regions. The Gaussian at ~ 2.1 keV was included to model the instrumental Au M complex discussed above. For both regions, the kT_1

¹² This instrumental issue is discussed at http://cxc.harvard.edu/cal/Acis/Cal_prods/qeDeg/index.html. The correction program and XSPEC model *acisabs* was developed by G. Chartas and is available at <http://www.astro.psu.edu/users/chartas/xcontdir/xcont.html>.

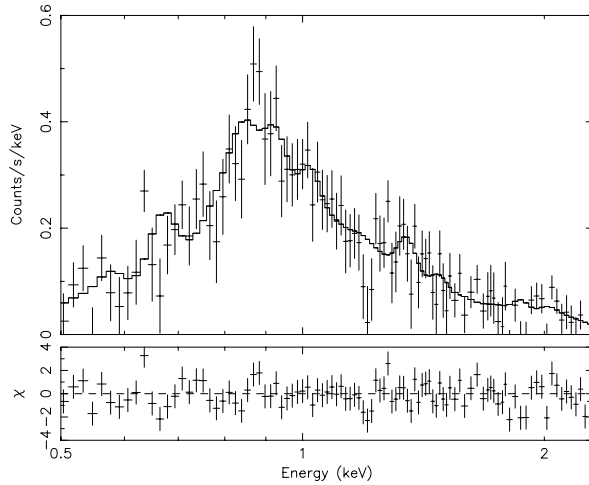


FIG. 9a

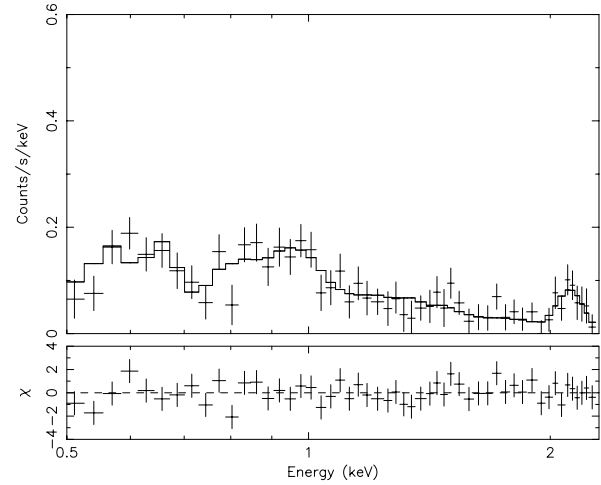


FIG. 9b

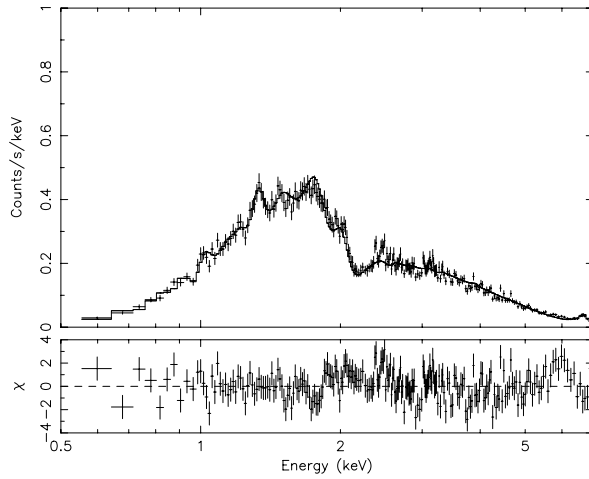


FIG. 9c

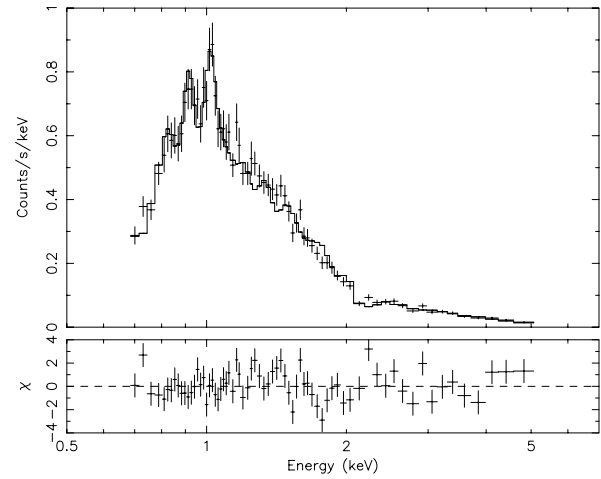


FIG. 9d

FIG. 9.—ACIS spectra of the following composite components using the spectral models given in Table 2. (a) M17 diffuse emission. (b) Rosette diffuse emission. (c) M17 point sources. (d) Rosette point sources. The top panels show the data and best-fit models; the bottom panels give the (data – model) residuals.

component was fixed to solar abundances while the kT_2 component was a variable-abundance plasma.

For comparison with the diffuse emission, we performed similar spectral fits on the emission from the combined point sources detected in the H II regions. Again the kT_1 component was fixed to solar abundances while the abundances for the kT_2 component were allowed to vary. The Rosette composite point source spectrum was adequately fitted by

plasmas at 0.2 and 2.1 keV with a single absorbing column. Fitting the combined M17 point sources required a more complicated model: a solar-abundance thermal plasma at 0.19 keV with a relatively low absorption ($7 \times 10^{21} \text{ cm}^{-2}$) and a variable-abundance thermal plasma (3 keV) with higher absorption ($17 \times 10^{21} \text{ cm}^{-2}$). This fit was also clearly improved by adding Gaussians at 1.1, 1.3, and 6.7 keV; lines at these energies are seen in O stars and in flaring pre-

TABLE 2
X-RAY SPECTRA AND LUMINOSITIES

TARGET	COUNTS	SCALED BACKGROUND COUNTS	ABSORPTION (10^{21} cm^{-2})		PLASMA TEMPERATURE (keV)		GAUSSIANS (keV)	X-RAY LUMINOSITIES ($10^{33} \text{ ergs s}^{-1}$)				REDUCED χ^2
			$N_{\text{H},1}$	$N_{\text{H},2}$	kT_1	kT_2		L_{soft}	L_{soft}^c	L_{hard}	L_{hard}^c	
M17 diffuse	19700	~9700	4 ± 1	...	0.13 ± 0.02	0.6 ± 0.1	2.1	0.4	3.4	1.2
Rosette diffuse.....	7800	~4500	2 ± 1	...	0.06 ± 0.02	0.8 ± 0.1	2.1	0.2	0.6	0.7
M17 point sources.....	36600	...	7 ± 1	17 ± 1	0.19 ± 0.02	3.0 ± 0.1	1.1, 1.3, 6.7	0.6	6.1	3.5	4.1	1.5
Rosette point sources.....	9500	...	6 ± 1	...	0.20 ± 0.02	2.1 ± 0.2	...	0.6	7.4	0.6	0.7	1.6

main-sequence stars (e.g., Schulz et al. 2000; Tsuboi et al. 1998). No line was needed to model the instrumental Au M complex in the combined point source spectra, indicating that no significant residual instrumental background is present around 2 keV.

In addition to the introduction of Gaussian lines, we found that extrasolar abundances of oxygen were needed to give a good fit to all of the spectra, and extrasolar abundances of neon were needed for the point-source spectra, although the actual abundance values were not well constrained. If both plasma components are forced to have solar abundances in the M17 spectra, the fits are statistically worse. The reduced χ^2 for the diffuse spectrum increases from 1.2 to 1.4; the plasma temperatures did not change, but N_{H} increased from 4×10^{21} to 6×10^{21} cm $^{-2}$. For the composite point source spectrum, the reduced χ^2 went from 1.5 to 3.7; the two absorption values and the first plasma component's temperature stayed the same, but the second plasma component increased from $kT_2 = 3.0$ to $kT_2 = 3.6$ keV. This caused the iron line to be too strong (even with elimination of the Gaussian at 6.7 keV) and was the major reason for the unacceptable fit.

Similar results were obtained for Rosette. Requiring both plasma components to have solar abundances in the fit to the diffuse spectrum caused the reduced χ^2 to increase from 0.7 to 1.3. As for M17, the plasma temperatures did not change, but N_{H} increased, here from 2×10^{21} to 5×10^{21} cm $^{-2}$. For the composite point source spectrum, the reduced χ^2 went from 1.6 to 3.0; the absorption stayed the same, but both plasma components increased in temperature: kT_1 went from 0.20 to 0.29 keV and kT_2 went from 2.1 to 2.9 keV. This caused large residuals below 2 keV; the model appeared to have many more linelike peaks than the data.

There are several reasons why including nonsolar abundances might improve the fit to these composite spectra. Excess Ne ix and Ne x lines are prominent in the spectra of nearby flaring late-type stars (Brinkman et al. 2001) and can be present in pre-main-sequence flaring stars as well. The origin of excess oxygen is less clear. We suspect that it is not astrophysically real but arises from inadequate modeling of the absorption. Each spectrum covers stars or regions with a wide range of foreground absorptions, leading to a confused observed spectrum in the less than 1 keV region, where oxygen has strong lines. The Gaussians needed to fit the M17 composite point source spectrum and other features seen in the (data – model) residuals in Figure 9 may also arise from the merging of different plasma conditions into a single spectrum. Imperfect background removal accounts for the residuals at low and high energies.

5.2. Spectral Results

The resulting plasma spectra are shown in Figure 9, and the parameters of the best-fit plasma models are given in Table 2. The L_{soft} values are the soft-band (0.5–2 keV) X-ray luminosities assuming distances of 1.6 kpc for M17 and 1.4 kpc for the Rosette Nebula; absorption-corrected values are given as L_{soft}^c . There is substantial hard-band (2–7 keV) flux only for the M17 combined point sources, where the absorption-corrected luminosity is $L_{\text{hard}}^c \simeq 4.1 \times 10^{33}$ ergs s $^{-1}$. The temperatures of both diffuse-emission plasma components are very similar in the two regions and are dominated by the $T \sim 10$ MK component, with a secondary 1 MK component. However, the regions are notably differ-

ent in luminosity and surface brightness, with the M17 diffuse emission a factor of greater than 5 brighter than the Rosette diffuse emission and coming from an extraction area $\sim 90\%$ as big as that used to sample the Rosette diffuse emission (roughly 42 pc 2 vs. 47 pc 2). Equivalently, we see that the diffuse component comprises $\simeq 36\%$ of the total soft luminosity in the M17 region sampled but only $\simeq 7\%$ in the Rosette Nebula region.

To within the errors, our kT_2 plasma component is consistent with the Dunne03 results from spectral modeling of the *ROSAT* data on M17. This is somewhat remarkable, since the *Chandra* data have shown that point sources contribute substantially to the X-ray emission in the *ROSAT* band. Our value for N_{H} is substantially larger than the Dunne03 value for their Regions A and C but is consistent with their N_{H} for Region D. The large section of the ACIS field that was used to sample the diffuse emission encompasses most of Dunne03 Regions C and D and part of their Region A, but it also extends farther to the north and west than those regions, into parts of the nebula that are more highly absorbed. This may account for our higher N_{H} estimate.

No hard diffuse component was detected in either ACIS field, when all diffuse counts were combined into a single spectrum. The smoothed X-ray images in Figures 3c and 4b–4d suggest that a diffuse hard component might be present in M17, toward the M17 Southwest molecular cloud and M17 North protostellar region. However, this emission is spatially coincident with high concentrations of point sources and, once those point sources are removed from the data, few hard counts are left to contribute to the global diffuse spectrum (see the swiss-cheese image, Fig. 4a).

There are enough diffuse counts in M17 to warrant subdividing them into smaller regions to search for spatial gradients in temperature. Two such schemes are shown in Figure 8, one sensitive to temperature effects associated with proximity to the molecular boundaries of the H II region cavity, and the other sensitive to cooling as the gas flows eastward from the central O stars. In almost all cases, no changes in plasma components were found. The only discrepant case is the westernmost box in Figure 8b, which showed 2.3 and 23 MK (0.2 and 2 keV) components (plus stronger absorption, with $N_{\text{H}} = 14 \times 10^{21}$ cm $^{-2}$). These properties may reflect either a change in plasma conditions or contamination by an unresolved population of lower mass stars (see § 6.2).

Finally, we note that the composite spectra of the point sources are complex in different ways (Fig. 9). Even complicated spectral models do not give statistically acceptable fits. This is understandable given that we have combined hundreds of different stars, each of which suffers different absorption and may have spatially and temporally variable plasma emission, to generate these composite spectra. The presence of excess neon and the iron line at 6.7 keV supports the interpretation that these are magnetically active flaring stellar sources. A soft ($kT \sim 0.2$ keV) spectral component is seen in the composite point source spectra of both M17 and Rosette; this may be simply a component of the stellar plasma, although Wolk et al. (2002) see a similar soft component in extended emission in RCW 38 and note that it may be partially caused by X-ray halos around the point sources, due to dust scattering. In any case, we have no evidence that the physical mechanism generating this soft plasma component in the stellar spectra is related to the soft

component seen in the diffuse emission. The most important result for our purposes here is that in both star-forming regions the point sources are dominated by a substantially harder plasma component (2–3 keV, or 23–35 MK) than seen in the diffuse emission (~ 0.7 keV, or 8 MK).

5.3. Physical Properties of the Plasma

It is clear from the above analysis that the diffuse X-ray emission in both the Rosette Nebula and M17 is due predominantly to a hot plasma. The physical parameters can readily be estimated, with results summarized in Table 3.

For both nebulae, our *Chandra* results show relaxed center-filled morphologies (§ 4). M17 lacks any measurable temperature gradients (§ 5), although Figure 5 hints that such gradients may be present; too few diffuse counts are present in our Rosette observation to search for such gradients. We therefore consider the simple situation of a uniform, optically thin, isothermal plasma in a simple geometry. For simplicity, we assume that the diffuse X-ray luminosities given in Table 2 come from the idealized emitting regions defined below; in reality, of course, the emission has a more complex structure.

For M17, we adopt a cylindrical geometry viewed perpendicular to its axis with radius $3/5$ ($r = 1.6$ pc) and length $8/7$ ($l = 3.7$ pc), giving a plasma volume $V_X = \pi r^2 l = 9 \times 10^{56}$ cm³. For the plasma volume V_X in Rosette, the emitting region can be approximated by a circle of radius $4/7$ ($r = 1.9$ pc), and we adopt a spherical geometry with volume $V_X = (4/3)\pi r^3 = 9 \times 10^{56}$ cm³. We introduce a geometric correction factor η of order unity to account for the possibility that the emitting regions are flattened or elongated along the line of sight. This is simultaneously used as a filling factor ($\eta < 1$) if the plasma density is inhomogeneous because of shocks or the penetration of cooler gas. We thus retain η as a free scaling parameter of the inferred physical parameters of the X-ray gas but find that most quantities depend only weakly on η . Recall that the true X-ray luminosity and emitting volume are undoubtedly larger than used here (probably by a factor of >2 for M17 and <2 for Rosette), since we restrict our diffuse photon extraction to regions with high surface brightness.

The plasma luminosities $L_{X,\text{bol}} = \beta L_X$ considered here scale the absorption-corrected X-ray luminosities given in Table 2 by a bolometric correction factor $\beta \simeq 1.3$ for $kT = 0.6$ – 0.8 keV to account for emission lying outside of the *Chandra* spectral band. Although the best-fit spectra are multitemperature, for simplicity we consider here the plasmas to be isothermal at the dominant energy around $kT = 0.7$ keV.

From the three measured quantities $L_{X,\text{bol}}$, V_X , and T_X , the basic physical parameters of the plasma can be derived. The plasma electron density $n_{e,X}$ is obtained from $L_{X,\text{bol}} = \Lambda n_{e,X}^2 \eta V_X$ ergs s⁻¹, where $\Lambda = 5 \times 10^{-23}$ ergs cm³ s⁻¹ is the bolometric X-ray emissivity for a cosmic abundance plasma at $kT_X = 0.7$ keV based on the CHIANTI emission-line database (Landi & Landini 1999); Λ is only weakly dependent on temperature close to $kT_X \approx 1$ keV. For a fully ionized cosmic abundance plasma, the mean molecular weight per electron is $\mu_X = 0.62$. Knowing $n_{e,X}$ and T_X , the plasma pressure is then $P_X/k = \rho T_X / (\mu_X m_p) = 2.2 n_{e,X} T_X$, the thermal energy $E_X = (3/2) P_X V_X$, and the cooling timescale $\tau_{\text{cool}} = E_X / L_{X,\text{bol}}$. The total mass of the X-ray gas is $M_X = \mu_X m_p n_{e,X} V_X$. The timescale for

TABLE 3
PHYSICAL PROPERTIES OF THE H II REGION PLASMAS

Parameter	Scale Factor	M17	Rosette
Observed X-Ray Properties			
kT_X (keV)	0.6	0.8
$L_{X,\text{bol}}$ (ergs s ⁻¹)	4×10^{33}	8×10^{32}
V_X (cm ³)	η	9×10^{56}	9×10^{56}
Derived X-Ray Plasma Properties			
T_X (K)	7×10^6	9×10^6
$n_{e,X}$ (cm ⁻³)	$\eta^{-1/2}$	0.3	0.1
P_X/k (K cm ⁻³)	$\eta^{-1/2}$	5×10^6	2×10^6
E_X (ergs)	$\eta^{1/2}$	9×10^{47}	3×10^{47}
τ_{cool} (yr)	$\eta^{1/2}$	7×10^6	1×10^7
M_X (M_\odot)	$\eta^{1/2}$	0.15	0.04
Derived Photodissociation Region Properties			
$n_{e,\text{II}}$ (cm ⁻³)	10^3	10^3
T_{II} (K)	8000	6400
P_{II}/k (K cm ⁻³)	1×10^7	9×10^6
O Star Wind Properties			
Stellar age t_* (yr)	1×10^6	2×10^6
$\Sigma(\dot{M}_w)$ (M_\odot yr ⁻¹)	3×10^{-5}	1×10^{-5}
$\Sigma(\dot{M}_w) t_*$ (M_\odot)	30	20
E_w (ergs)	9×10^{48}	2×10^{48}

NOTES.—The term η is a multiplicative factor for the volume of the emitting plasma, correcting the observed volume to the actual volume, taking extinction, possible inhomogeneities, etc., into account. Note that all derived plasma properties, being $\propto \eta^{1/2}$, are not very sensitive to this correction. See § 5.3 for details.

dynamical equilibration across the X-ray regions is $\tau_{\text{equil}} = r/v_s \simeq 1 \times 10^4$ yr, where $v_s = 0.1 T_X^{1/2}$ km s⁻¹ is the plasma sound speed. This short equilibration timescale indicates that the X-ray plasma should quickly fill most of the H II region volume, supporting the assumption of a constant temperature over the X-ray-emitting region except where shocks are present. The X-ray morphologies of both regions are center-filled and roughly consistent with the uniform plasma assumed here, although deeper exposures may reveal inhomogeneities due to shocks.

In addition to providing these quantities for the M17 and Rosette X-ray-emitting regions in Table 3, we compare them with properties of the H II photodissociation regions that surround the X-ray gas based on published radio and optical studies. Note that at these lower temperatures helium is only partially ionized: Celnik (1985) gives $N(\text{He}^+)/N(\text{H}^+) = 0.12$ for the Rosette. Then the mean molecular weight per electron in the photodissociation region is $\mu_{\text{II}} = 0.95$, and $P_{\text{II}}/k = 1.4 n_{e,\text{II}} T_{\text{II}}$. We also assume $\eta = 1$ for this H II gas, which may not be correct if the warm gas is filamentary, as suggested by recent high-resolution optical and infrared images (Jiang et al. 2002). We use the values of T_{II} and $n_{e,\text{II}}$ given in Tsivilev et al. (2002) for Rosette.

We can first compare the gas pressures of the X-ray and H II regions. In M17, the X-ray plasma and photodissociation region pressures are approximately equal, so that the plasma probably does not expand radially, perpendicular to the axis of the H II cylinder. Unfortunately, the H II pressure in the low-density side east of this cylinder is unmeasured,

but it is possible that the X-ray plasma is unconfined and expands in that direction. The similarity between the radio, optical, and *ROSAT* images (Fig. 1) would, however, suggest that it is at least partially confined. We can compare our estimate of T_X and $n_{e,X}$ to the *ROSAT* results for M17: Dunne03 find $T_X = 8.5 \times 10^6$ K and $n_{e,X} = 0.09 \text{ cm}^{-3}$. The X-ray temperatures are comparable to within the errors, but the density is somewhat lower; this is expected because the *ROSAT* data sample the fainter, more extended emission eastward of the ionizing cluster that is missed in the smaller ACIS-I FOV.

Rosette is similar: the nominal pressure of the X-ray plasma is the same as the photodissociation region pressure, if we assume that the model of Tsivilev et al. (2002) is correct and the inner shell contains high-density clumps ($n_{e,II} = 10^3 \text{ cm}^{-3}$). However, there is still a difficulty in explaining why the Rosette cavity is much smaller than it should be according to standard bubble models (§ 7). There are two possible explanations here: either the plasma volume is greatly elongated along the line of sight so that $\eta \gg 1$ and the density is considerably lower than we estimate here, or the plasma escapes and flows into the surrounding interstellar medium. As mentioned above, this flow might be an unimpeded X-ray fountain roughly along the line of sight, as we clearly see in M17 nearly in the plane of the sky, and/or a leakage of X-ray gas through fissures in the H II and molecular gas.

6. POSSIBLE ORIGINS OF THE EXTENDED EMISSION

6.1. Instrumental Effects

We are quite confident that the extended emission does not arise from some instrumental effect. For each source, the *acis_extract* procedure (§ 3) calculates the polygon enclosing 99% of the PSF, then masks out a circular region 1.1 times larger than the largest chord of this polygon to create the swiss-cheese image. Thus, we have been very careful to remove all of the emission from detected point sources, accounting for the size and shape of the PSF at different locations on the detector. Residual contamination from known point sources should therefore contribute negligibly to the measured diffuse emission (Table 2).

There are no known spatial variations in the background events in the ACIS-I array that mimic either the M17 or Rosette diffuse emission. As discussed in § 5.1, a temporal flare occurred during the Rosette observation but had little effect on the soft band where the diffuse emission appears; flare events also should be distributed roughly uniformly across the detector.

6.2. Low-Mass Pre-Main-Sequence Stars

There is a more serious concern that a large number of cluster members that are too faint to be individually detected as point sources may mimic diffuse emission. This indeed was a significant problem with the earlier *Einstein* and *ROSAT* studies of HMSFRs (§ 1). We can quantitatively evaluate this effect by comparing the M17 and Rosette clusters to the ONC and its environs, for which there is both a more complete stellar census and deeper *Chandra* X-ray coverage than for the clusters considered here (Feigelson et al. 2002, see their Tables 2, 3, and 5). We assume here that the ONC, M17, and Rosette stellar clusters have identical initial mass functions with identical X-ray luminosity functions, differing only in their total population. Since M17 and

Rosette have 51 and up to 31 members, respectively, with spectral type B3 or earlier (if we assume that most stars listed in Table 6 are members of NGC 2244), compared to eight high-mass stars in the ONC, we infer that they have ~ 6 and ~ 4 times the low-mass population of the ONC. The ONC has 1075 *Chandra* detections above 0.10 counts ks^{-1} in the ACIS-I detector. Our sensitivity to point sources in the M17 and Rosette fields, scaling by both exposure time and distance, is equivalent to sensitivities of 2.7 and 4.0 counts ks^{-1} , respectively, in the ONC. Examining the ONC source count distribution and scaling upward by factors of 6 and 4 to match the overall cluster populations, we predict the detection of 1960 sources in M17 and 900 sources in Rosette. This is about a factor of 2 higher than the number of sources detected in M17 and in Rosette Field 1. However, since many of the ONC sources are from an embedded population behind the H II region, while in M17 and Rosette these embedded stars are mainly displaced from the H II region, we believe this difference is not significant.

Having established that the detected ONC, M17, and Rosette source counts are at least roughly compatible, we now use the deeper ONC observation to obtain the coarse estimate that 4500 and 6100 undetected sources emitting 3×10^{32} and 5×10^{32} ergs s^{-1} should be present in the M17 and Rosette Fields, respectively (more Rosette sources remain undetected mainly because our observation of Rosette Field 1 is half as long as our M17 observation). This is about 8% and 80% of the absorption-corrected diffuse X-ray luminosity L_{soft}^c shown in Table 2. For M17, this result clearly supports the already convincing morphological evidence that very little of the “diffuse” emission can arise from the undetected population of X-ray-faint cluster members. The situation is not quite so clear for Rosette, where our calculation permits that a significant fraction, even most, of the “diffuse” emission could come from undetected stars; note that this calculation is very rough, though, and could easily be in error by a factor of 2. The difference in spectral shape between the “diffuse” and the detected point source components (compare Figs. 9b and 9d), however, independently indicates that the point-source contribution to the diffuse emission is small. The issue will be easily settled with the upcoming deeper *Chandra* observation of Rosette: from the ONC source count distribution, we estimate that a 100 ks exposure should resolve about half of the emission from stars that are currently undetected.

6.3. Supernova Remnants

In M17, there are many arguments against a hypothesis that the X-rays are independent of the H II gas and instead arise from the remnant of a recent supernova explosion. Foremost, the X-ray morphology follows very closely the morphology of the thermal radio and optical emitting H II region (§ 4.1), which does not show kinematic disturbances greater than $\simeq 100 \text{ km s}^{-1}$. In addition, the stellar cluster currently has no stars evolved off of the main sequence, indicating a young age, and is insufficiently rich to host a population of extremely massive stars that could evolve extremely rapidly into a supernova. Even in a cluster with 100 O stars, the first supernova explosion does not occur for $\simeq 4$ Myr (Knödseder et al. 2002). There is no report of polarized nonthermal radio emission in the region despite many studies (although conceivably nonthermal emission from a small SNR could be absorbed by free-free processes

in the H II gas). The only hints of energetic activity that could be associated with a SNR are several arclike structures seen in the optical and low-frequency radio images and some high-excitation optical emission lines (§ 2.1), but the latter cannot be SNRs because there are no corresponding X-ray enhancements in the *ROSAT* image (see the simulations of Velázquez, Koenigsberger, & Raga 2003).

The issue is somewhat more complicated for the Rosette Nebula because of the presence of the large Monoceros Loop, a well-known old SNR, in its vicinity (§ 2.2). However, the Monoceros Loop is far larger than the Rosette and is displaced, in the plane of the sky and probably also along the line of sight, from the region we study here. Furthermore, the X-ray morphology of the nebula is center-brightened and nicely fills the hole within the toroidal H II emission. Most SNRs are either edge-brightened with thermal spectra or plerionic with nonthermal spectra; only a handful are known that are center-filled with thermal gas. Finally, we recall that, like M17, the NGC 2244 cluster is too young (1.9 Myr; § 2.2) and too poor to plausibly have produced a SNR.

We conclude that in both M17 and the Rosette Nebula the interpretation of the diffuse emission as arising from the interior or shock of a SNR can be ruled out with considerable confidence.

6.4. O Star Winds

To investigate whether the properties of the plasma derived in § 5.3 are consistent with an origin in the O star winds, we apply the stellar wind properties obtained from ultraviolet P Cygni lines for large samples of O stars (Howarth & Prinja 1989) to the O stellar populations of the two clusters under study (see Appendix A). Specifically, we apply the empirical relation $\log \dot{M} = 1.69 \log(L_*/L_\odot) - 15.41$, converting spectral subtypes to bolometric L_* following Panagia (1973). This gives estimated total mass-loss rates of $\Sigma(\dot{M}_w) \sim 3 \times 10^{-5}$ and $1 \times 10^{-5} M_\odot \text{ yr}^{-1}$ for the M17 and Rosette ionizing clusters, respectively.

The derived X-ray emitting plasma masses (Table 3) can thus be replenished by winds in $t_w \sim 5000$ yr for M17, $t_w \sim 4000$ yr for Rosette. Since this is much shorter than the lifetime of the OB stars, we infer that only a tiny fraction of the wind material generated over the OB star lifetimes is now in X-ray-emitting plasma. A typical early O star wind with terminal velocity $v_w = 2500 \text{ km s}^{-1}$ would travel $r_w = v_w t_w = 12.8$ pc in M17 (10.2 pc in Rosette) during the replenishment timescale. This wind kinetic timescale t_w is also much shorter than the plasma cooling timescale τ_{cool} , consistent with the absence of any strong cooling in the plasma as a function of distance from the O stars. Most importantly, we find that the wind kinetic energy $E_w \sim \frac{1}{2} \Sigma(\dot{M}_w) v_w^2 t_w$ is 10 and 7 times the plasma thermal energy estimated above for M17 and Rosette, respectively. Thus, only $\sim 10\%$ of the wind energy need be converted via shocks into hot thermal plasma to account for the observed X-ray emission.

7. ELABORATION OF THE OB WIND BUBBLE MODEL

From the analysis above, we find that the only plausible origin for the ~ 0.7 keV (8 MK) diffuse emission suffusing the M17 and Rosette H II regions is the thermalization of O

star wind kinetic energy. Our findings thus support the basic concept of shocked windswept bubbles (e.g., Pikel'ner 1968; Dyson & de Vries 1972; Weaver et al. 1977) and provide some of the first clear detections of X-ray temperature plasma in H II regions.

The calculations in § 6.4 with respect to a simple wind shock model show that only about 10% of the expected wind kinetic energy is converted into observed thermal energy. The shocked wind bubbles in M17 and Rosette are less than 10 pc in radius. For comparison, the hydrodynamic calculation of Weaver et al. (1977) predicts, for a *single* $t_* = 1$ Myr O7 star expanding into a uniform cold medium, that 30% of the wind energy appears in the X-ray temperature gas, which has a typical radius of 25 pc. Similar discrepancies are found between the relatively low displacement velocities in H α found in recently studied LMC H II regions (Nazé et al. 2001). Thus, most of the wind kinetic energy is not seen in the X-ray gas and does not expand the bubble.

Several ideas have been raised to account for the missing energy and momentum of OB winds. The most obvious possibility, for blister H II regions that are only partially confined by cold gas, is that the hot gas flows freely into the low-density interstellar medium, away from the cloud. Hydrodynamic models of the expansion of stellar wind bubbles in the presence of strong density gradients are presented by Różyczka & Tenorio-Tagle (1985) and Comerón (1997). A flow of this type is directly seen in our X-ray image of M17, where the X-rays extend asymmetrically several parsecs to the east, and may also be present in the Rosette Nebula, where gas may flow nearly along the line of sight or through fissures in the inhomogeneous cold cloud. In the latter case, the hot medium probably quickly mixes with cloud material and becomes subject to rapid radiative cooling (McKee et al. 1984; Capriotti & Kozminski 2001).

Another possible sink for wind kinetic energy is its conversion into a turbulent cascade in a thick boundary layer where the wind approaches the cold medium (Kahn & Breitschwerdt 1990). In this case, a high-velocity shock producing X-ray plasma is weak and most of the wind energy is eventually radiated at longer wavelengths. The soft $kT \simeq 0.1$ keV (1 MK) component seen in the Rosette and M17 diffuse emission (Table 2) may be direct evidence for rapid cooling in a postshock or turbulent boundary layer.

A related possibility is that the wind loses most of its kinetic energy through the entrainment of cooler material close to the star (e.g., Arthur, Dyson, & Hartquist 1993; Dyson, Williams, & Redman 1995; Pittard et al. 2001). While mass loading close to the star is unlikely in these mature H II regions that have evacuated molecular material within the stellar association, this process may be occurring at the boundaries between the X-ray and cooler gases. In the Rosette, optical images show elephant trunk structures that might be good sites for ablation and entrainment. In M17, the stellar winds may be encountering a fissured neutral medium in the highly fragmented southern H II bar (e.g., Clayton et al. 1985; Meixner et al. 1992).

Another possibility is that the X-ray gas is produced, and the kinetic energy spent, primarily in collisions between the OB winds rather than with the exterior cold cloud. Cantó et al. (2000) present a three-dimensional hydrodynamic calculation of colliding OB winds that are otherwise unconfined by dense cold gas. This is an attractive model for our data, since it immediately accounts for the center-filled rather than edge-brightened morphology of the X-ray

emission and for the bulk flow of the merged, shocked winds into the diffuse medium seen in M17. They find that the X-ray emission measure integrated along the line of sight produces rather uniform emission filling the center of the cluster, even though strong pressure gradients are present at the wind-wind collision shocks. The gas temperatures over the inner parsec of the cluster are in the range 5–10 MK, essentially identical to the temperatures found here for the M17 and Rosette diffuse emission.

We finally note that we do not have any clear evidence for very hard diffuse X-ray emission that might emerge from non-Maxwellian particle acceleration at a wind-cloud shock (Dorland & Montmerle 1987). The smoothed ACIS image of M17 suggests that a hard (blue) diffuse component may be present where the hot bubble encounters the M17 Southwest molecular cloud (Figs. 3*a* and 3*c*), but the emission is not evident in the swiss-cheese image after point sources have been removed (Fig. 4*a*). Our adaptive smoothing tool also shows hints of diffuse hard emission near the cluster core and the young embedded star-forming region M17 North (Figs. 4*b–d*), but again this is more likely to be unresolved emission from embedded point sources in these regions.

8. X-RAYS FROM HIGH-MASS STAR FORMING REGIONS

8.1. Summary of High-Mass Star Forming Region X-Ray Results to Date

We place the M17 and Rosette results in the broader context of diffuse X-ray characteristics of other Galactic star-forming regions to seek an understanding of the conditions necessary for large-scale X-ray-emitting OB wind shocks. Results from recent *Chandra* and *XMM-Newton* observa-

tions (and one older *Einstein Observatory* result) are summarized in Table 4, listed in order of increasing reported diffuse X-ray luminosity. We caution that this should be considered a progress report rather than an authoritative tabulation.¹³ The regions are subject to different levels of absorption, were observed with different sensitivities (in ergs s⁻¹) and resolution (in pc), and were subject to different treatments of the T Tauri X-ray source population and diffuse emission. In most regions, the underlying T Tauri population is poorly characterized, and in some regions even the OB stars are not fully identified.

Nearby low-mass star forming regions (LMSFRs).—Here we bundle together recent high-resolution studies of the Taurus-Auriga, Ophiuchi, and Perseus molecular clouds (e.g., Imanishi, Koyama, & Tsuboi 2001; Preibisch & Zinnecker 2001; Getman et al. 2002; Favata et al. 2002), along with a region of low-density star formation in the Orion cloud (Pravdo et al. 2001). Two cases of faint 10²⁸ ergs s⁻¹ diffuse (i.e., from interstellar gas rather than the immediate vicinity of young stars) X-ray emission with an extent of less than 10⁻³ pc have been found in these regions, associated with small-scale shocks in high-velocity Herbig-Haro outflows (Pravdo et al. 2001; Favata et al. 2002; Bally, Feigelson, & Reipurth 2003). No stars earlier than late B are present in these images, and none of these studies report diffuse X-ray emission on parsec scales. The sensitivity limit to such emission is of order 10²⁹ to 10³⁰ ergs s⁻¹ pc⁻², or 10⁻³ to 10⁻² of that seen here in M17 and the Rosette.

Orion Nebula (M42).—With its “Trapezium” of the O6 star θ^1 C Ori surrounded by a group of O7 V to B0 V stars, a full initial mass function down to the brown dwarf regime,

¹³ Earlier versions of this table were presented at conferences by Feigelson (2001) and Townsley et al. (2003).

TABLE 4
DIFFUSE X-RAYS FROM HIGH-MASS STAR FORMING REGIONS

Region	Distance (pc)	Earliest Star ^a	Number O6 or Earlier	Diffuse X-Rays?	Diffuse Area (pc ²)	N_H (10 ²¹ cm ⁻²)	kT (keV)	L_X^b (10 ³³ ergs s ⁻¹)	Ref.
LMSFRs ^c	150–350	Late B	0	No	$\leq 10^{-5}$...
Orion Nebula	450	O6	1	No	$< 10^{-3}$	1
Eagle Nebula	2000	O5	2:	$< 10^{-3}$	2
Lagoon, NGC 6530	1800	O4	3:	No	$< 10^{-2}$	3
Lagoon, Hourglass	1800	O7	0	Probably	0.04	11.1	0.63	$\leq 0.7^d$	3
Rosette Nebula	1400	O4	2	Yes	47	2	0.06, 0.8	$\leq 0.6^d$	4
RCW 38	1700	O5	1:	Yes	2	11.5 ^e	2.2 ^e	1.6 ^e	5
Omega Nebula ^f	1600	O4	7	Yes	42	4	0.13, 0.6	3.4	4
Arches cluster	8500	O3/W-R	>30	Yes	14	100	5.7	16	6
NGC 3603	7000	O3/W-R	>20	Yes	50	7	3.1	20	7
Carina Nebula	2300	O3/W-R	>30	Yes	1270	3–40	0.8:	200:	8

^a Some of these regions contain heavily obscured ultracompact H II regions or high-mass protostars, so the “earliest star” is approximate. We list here the earliest spectral type given in the literature.

^b Luminosities are obtained from the listed reference. They are corrected for absorption and usually cover the 0.5–2 keV band for soft emission, the 2–8 keV band for hard emission. For diffuse emission that extends beyond the ACIS-I FOV, these are lower limits. The X-ray luminosity in LMSFRs refers to two cases of diffuse X-rays from Herbig-Haro outflow shocks.

^c Low-mass star formation regions near the Sun such as the Taurus-Auriga, Ophiuchi, Chamaeleon, Lupus, and Perseus clouds. Very faint and localized regions of diffuse X-rays have been found in two young stellar outflows; see text.

^d The upper limits here refer to likely contributions from unresolved stellar X-ray sources.

^e Thermal plasma fit to the core of the diffuse emission; the authors prefer a power law plus thermal plasma fit, with $N_H = 9.5 \times 10^{21}$ cm⁻², $\Gamma = -1.6$, and $kT = 0.2$ keV for the total diffuse emission. We estimated L_X from these parameters using PIMMS (<http://xte.gsfc.nasa.gov/Tools/w3pimms.html>).

^f Values for area, N_H , kT , and L_X are determined from the ACIS data. Additional diffuse soft X-rays are seen in the *ROSAT* data, outside the ACIS FOV; including this emission would roughly double the area and increase L_X by $\sim 1 \times 10^{33}$ ergs s⁻¹ (Dunne03).

REFERENCES.—(1) Feigelson et al. 2002; (2) Mytyk et al. 2001; (3) Rauw et al. 2002; (4) this work; (5) Wolk et al. 2002; (6) Yusef-Zadeh et al. 2002; (7) Moffat et al. 2002; (8) Seward & Chlebowski 1982.

and an embedded cluster associated with the OMC-1 core, the Orion Nebula is the nearest HMSFR and a bright H II region. θ^1 C Ori is the principal ionizing source of the H II region and has a wind with mass-loss rate $\dot{M} = 8 \times 10^{-7} M_{\odot} \text{ yr}^{-1}$ and terminal velocity $v_{\infty} = 1650 \text{ km s}^{-1}$ (Leitherer 1988). In extensive studies with *Chandra*, no diffuse emission has been reported (e.g., Schulz et al. 2001; Feigelson et al. 2002; Flaccomio et al. 2003). The upper limit to parsec-scale emission is around $10^{30} \text{ ergs s}^{-1} \text{ pc}^{-2}$. Note, however, that the O6 star is extremely bright in X-rays and populates the wings of its PSF, so that faint diffuse emission could go unnoticed in the inner $\approx 0.4 \text{ pc}$ radius.

Eagle Nebula (M16).—A 77 ks *Chandra* image of this region reveals over 1000 point sources, most associated with the ionizing cluster NGC 6611 (Mytyk et al. 2001). The earliest stars in the cluster (Hillenbrand et al. 1993) are the O5.5 V((f)) star BD $-13^{\circ}4923$ and HD 168076 [O5 V((f)), $v_{\infty} = 3305 \text{ km s}^{-1}$, $\dot{M} = 3 \times 10^{-6} M_{\odot} \text{ yr}^{-1}$]. (For this and the following O stars, we have taken terminal wind velocities v_{∞} from Prinja, Barlow, & Howarth 1990 and mass-loss rates \dot{M} from Howarth & Prinja 1989, both based on studies of ultraviolet line profiles.) Our inspection of the M16 ACIS image reveals no obvious diffuse emission at levels greater than $\sim 10^{30} \text{ ergs s}^{-1}$, although detecting any faint diffuse emission spatially coincident with the large number of point sources in the image would require more careful analysis.

Lagoon and Hourglass Nebulae (M8).—The bright bipolar H II region in M8 known as the Hourglass Nebula was studied with *XMM-Newton* by Rauw et al. (2002). Although limited by its small extent and confusion with embedded stellar sources, soft diffuse emission with luminosity $L_X \approx 7 \times 10^{32} \text{ ergs s}^{-1}$ and energy $kT = 0.6 \text{ keV}$ ($T = 7 \text{ MK}$) was “probably” detected from the southern lobe of the nebula. The diffuse plasma luminosity lies below this value since some contribution from the exciting star, Herschel 36 (O7 V), and lower mass stars is undoubtedly present. As we find here with M17 and Rosette, the authors note that this X-ray luminosity is far below the $10^{35} \text{ ergs s}^{-1}$ kinetic power of Herschel 36. An existing 60 ks *Chandra* observation of M8 did not include the Hourglass Nebula, but a 180 ks observation that includes the Hourglass is scheduled. The *XMM-Newton* image of the larger M8 region shows no diffuse emission associated with the main ionizing star, 9 Sgr (O4 V, $v_{\infty} = 2750 \text{ km s}^{-1}$, $\dot{M} = 5 \times 10^{-6} M_{\odot} \text{ yr}^{-1}$), and none is seen in our qualitative examination of the 60 ks *Chandra* image. Note that the other major ionizing stars of M8, HD 165052 (O6.5 V + O6.5 V binary, $v_{\infty} = 2295 \text{ km s}^{-1}$, $\dot{M} = 3 \times 10^{-7} M_{\odot} \text{ yr}^{-1}$), lie just outside the FOVs of both the *XMM-Newton* and *Chandra* observations.

Rosette Nebula.—This HMSFR is discussed in detail above, with OB stars listed in Appendix A. The area of diffuse emission listed here is the size of the extraction region used to obtain the diffuse spectrum (the full ACIS-I array). The diffuse emission is soft, with spectral components at 0.1 and 0.8 keV (1 and 9 MK) and with an absorption-corrected X-ray luminosity of $L_c \leq 6 \times 10^{32} \text{ ergs s}^{-1}$ (Table 2). The true plasma emission is less than the observed value because of the uncertain, but possibly substantial, contribution of unresolved T Tauri stars (§ 6.2). The H II region is mainly ionized by two stars with similar wind powers: HD 46223 [O4 V((f)), $v_{\infty} = 2910 \text{ km s}^{-1}$, $\dot{M} = 2 \times 10^{-6} M_{\odot} \text{ yr}^{-1}$] and HD 46150 [O5 V((f)), $v_{\infty} = 2925 \text{ km s}^{-1}$, $\dot{M} = 2 \times 10^{-6} M_{\odot}$

yr^{-1}]. Unlike the Trapezium and M17, where the O stars are concentrated within the inner $\approx 0.5 \text{ pc}$, the two dominant stars in Rosette are widely separated by at least 3 pc.

RCW 38.—Both soft and hard diffuse X-ray emission is reported from a 97 ks *Chandra* observation of this bright southern H II region (Wolk et al. 2002). Its ionization is dominated by a single O5 star, IRS 2. The authors fit the diffuse X-rays with a thermal bremsstrahlung plus power law model, attributing the soft bremsstrahlung component to dust-scattered X-rays and the hard power law component to some nonthermal magnetic process, perhaps synchrotron emission from an embedded SNR (see our discussion in § 6.3). We note, however, that the diffuse spectrum in RCW 38 is similar to the integrated point source spectrum we find in M17 (Fig. 9c). We fit the latter sources with a thermal plasma ($kT = 3.0 \text{ keV}$, $N_H = 1.7 \times 10^{22} \text{ cm}^{-2}$) similar to one that fits the RCW 38 diffuse emission ($kT = 2.23 \text{ keV}$, $N_H = 1.15 \times 10^{22} \text{ cm}^{-2}$ with low metal abundances; Wolk et al. 2002). The authors use a deep K-band image to argue that the diffuse emission does not arise from the low-mass pre-main-sequence population; it would be useful to make a comparison between the diffuse spectrum and the combined point source spectrum to elucidate the level of T Tauri contamination. We thus list in Table 4 the diffuse luminosity $L_X = 1.6 \times 10^{33} \text{ ergs s}^{-1}$ (which we estimated based on the count rates and spectral parameters reported in Wolk et al. 2002) as an upper limit to the diffuse emission generated by OB winds.

Omega Nebula (M17).—These results are also discussed in detail above, with OB stars listed in Appendix A. The area of diffuse emission listed here is the size of the extraction region used to obtain the diffuse ACIS spectrum (see Fig. 8a); the *ROSAT* data show that fainter, soft diffuse emission extends eastward for at least another 7 pc (see Fig. 1d and Dunne03, Fig. 2). The ACIS diffuse emission is soft like Rosette’s, with absorption-corrected $L_c = 3.4 \times 10^{33} \text{ ergs s}^{-1}$. Emission outside the ACIS FOV contributes another $\sim 1 \times 10^{33} \text{ ergs s}^{-1}$ (Dunne03). Here, spatial structure combined with spectral comparison shows negligible contamination by low-mass stars. The O stars in M17 lack direct measurements of v_{∞} and \dot{M} , but Dunne03 calculate these quantities using the method of Schaerer & de Koter (1997) and find $v_{\infty} = 2500\text{--}3000 \text{ km s}^{-1}$, $\dot{M} = (0.3\text{--}4) \times 10^{-6} M_{\odot} \text{ yr}^{-1}$ (see their Table 2). Ionization of the H II region is probably dominated by the obscured O4-O4 binary called Kleinmann’s Anonymous Star.

Arches cluster.—The Arches is one of three very massive and heavily obscured young stellar clusters in the inner 100 pc of the Galactic center. A 51 ks *Chandra* image shows a complex morphology: most of the emission comes from two structures in the interior of the core, which may arise either from localized wind-wind collisions from close binaries or from more extended wind shocks (Yusef-Zadeh et al. 2002). The third component (A3), with $L_X \sim 1.6 \times 10^{34} \text{ ergs s}^{-1}$, is clearly extended several parsecs away from the stellar association, similar to the flow we see in M17. It is this component that we list in Table 4 as a lower limit to the diffuse X-ray emission, for comparison with other regions. Note that the emission is considerably harder than that seen in Rosette or M17 (although the fit parameters are uncertain because of the small number of counts detected) and shows a strong 6.4 keV iron fluorescent line, suggesting close interaction between the winds and ambient molecular gas. The heavy obscuration along this line of sight precludes

detection of a soft component analogous to the M17 and Rosette diffuse emission.

NGC 3603.—This very dense and luminous massive stellar cluster, often considered to be the Galactic analog of the R136 cluster at the center of 30 Doradus in the Large Magellanic Cloud, lies at a distance similar to the Arches cluster but is less obscured. A 50 ks *Chandra* study shows hard diffuse emission with an extent of ≈ 8 pc with $L_X \approx 2 \times 10^{34}$ ergs s^{-1} and energy ranging from $kT = 2$ to 3 keV ($T = 23$ to 35 MK), in addition to nearly 400 point sources (Moffat et al. 2002). The diffuse component is spatially coincident with the cluster core, but the authors calculate that the underlying pre-main-sequence population should be too faint to contribute substantially to the emission. The diffuse emission is attributed to the collisions of multiple stellar winds from a large population of massive (including O3–5 V and W-R) stars in the region.

Carina Nebula.—Carina is a giant H II region extending over ~ 50 pc, with an extremely rich young stellar population. It is a complicated mix of several very rich star clusters of varying ages and evolutionary states, including many very massive O3 V stars, post-main-sequence W-R stars, and the unique eruptive η Car system. Early study with the *Einstein* satellite revealed pointlike emission from several early-type stars and a soft diffuse X-ray component, with $L_X \approx 10^{35}$ ergs s^{-1} extending over tens of parsecs (Seward & Chlebowski 1982). Dorland & Montmerle (1987) concluded that a substantial fraction of the *Einstein* emission at low energies (< 3 keV) could be explained by T Tauri stars similar to those seen in ρ Ophiuchus, while the hard X-ray contribution (> 3 keV) could be truly diffuse emission. Portions of the complex have been observed with *XMM-Newton* and *Chandra*; our examination of these images confirms the presence of diffuse emission with large-scale (> 5 pc) gradients that cannot be attributed to an unresolved low-mass stellar population. Evans et al. (2003) examine early *Chandra* data and conclude that over half of the X-ray emission in Carina might come from a diffuse component. However, given the presence of many evolved massive stars, it seems likely that one or more supernovae have occurred in the region. The relative contribution of SNRs and OB wind shocks to the diffuse X-ray component is, in our opinion, unknown.

Other regions.—Closely related observations have been made that, for reasons of insufficient knowledge, we omit from Table 4. A *Chandra* observation of the heavily obscured group of ultracompact H II regions in W3 showed over 200 point sources but no diffuse emission (Hofner et al. 2002). However, any soft emission with $kT \leq 1.5$ keV (17 MK) would be absorbed by intervening material. A faint X-ray structure with $kT \approx 6$ keV (70 MK) and $L_X \approx 10^{33}$ ergs s^{-1} has been detected with *Chandra* in a $1 \text{ pc} \times 1 \text{ pc}$ region within the Sgr B2 North H II region (Takagi, Murakami, & Koyama 2002). The absorption here is extremely high, with $N_H = 6 \times 10^{23} \text{ cm}^{-2}$ corresponding to over 100 mag of visual absorption. It is not possible here to discriminate between emission arising from individual massive stars, many low-mass stars, and wind shocks. X-ray emission has also been found with *ROSAT* and *ASCA* in regions such as W51, NGC 6334, and the Trifid Nebula; *Chandra* data have been recently obtained for these regions. Detailed analyses of the contribution from diffuse hot wind bubbles based on these new high-resolution images have not yet been reported, however.

8.2. Implications for X-Ray Emission from OB Wind Shocks and the Structure of H II Regions

Some tentative conclusions regarding the generation of parsec-scale X-ray gas in star-forming regions can be reached from these recent findings. Except for faint ($L_X \sim 10^{28}$ ergs s^{-1}) and localized ($< 10^{-3}$ pc) emission from some shocks in Herbig-Haro outflows (Pravdo et al. 2001; Favata et al. 2002), LMSFRs show no diffuse X-rays. The terminal shocks of T Tauri winds do not produce diffuse X-rays detectable with the current generation of X-ray observatories.

Weaver et al. (1977) and similar models of wind-blown bubbles predict measurable X-ray emission associated with a single O star, even a relatively late O7 star. However, the *Chandra* data show that the powerful 2000–3000 km s^{-1} winds of early O stars are clearly a necessary condition to produce the shocks responsible for diffuse soft X-ray emission. Abbott (1982) showed that stellar wind power is a strong function of spectral type; late O stars have wind power reduced by a factor of 5 from that of early O stars, so HMSFRs without stars earlier than O6 may be unlikely to exhibit diffuse soft X-rays. Also, the absence of such diffuse emission in the Orion, Eagle, and Lagoon Nebulae, where only one or two stars earlier than \sim O6 are present, suggests another discrepancy with the Weaver et al. (1977) prediction: the O stars must be sufficiently numerous to produce detectable diffuse X-rays. The proximity of the O stars may also be important: it is possible that colliding winds, as discussed by Cantó et al. (2000), may be more efficient at creating the kind of X-ray fountain we see in M17, with plasma flowing away from the exciting O star cluster.

The principal exception to these ideas is the Hourglass Nebula, where a single O7 star may have associated soft diffuse X-rays. Perhaps this star's youth and proximity to molecular material enhances the production of soft X-rays. For parsec-scale emission, the Rosette Nebula, with two widely separated O4–O5 stars and $L_X(\text{diffuse}) \sim 10^{32}$ ergs s^{-1} , may represent the minimal wind environment necessary to produce detectable diffuse soft X-rays. Even in this minimal case, the X-ray plasma appears to have a sufficiently strong dynamical effect to evacuate cooler material from the interior of the nebula, resulting in the annular structure of its H II gas.

The Omega Nebula, Arches cluster, and NGC 3603 cluster have richer O star populations, producing $L_X(\text{diffuse}) \sim 10^{33}–10^{34}$ ergs s^{-1} . Here the gas fills the interior of the photoionized H II region, pushing against the cold cloud material where it is present, and flowing away from the stellar cluster where it is not. In § 6.4 and Table 3, we give a quantitative analysis of this type of nebula. Less than 1% of the wind material produced over the history of the O stars is present in the nebula, suggesting that most of the wind has flowed outward, contributing to the Galactic hot interstellar medium. Some of the gas may cool, as evidenced by the 0.1 keV (1 MK) spectral component we see here. The X-ray gas in M17 is roughly in pressure equilibrium with the cooler H II gas. The Rosette data imply that soft X-rays are present without multiple O stars in close proximity. The diffuse emission of M17 is not concentrated around the O4–O4 binary system, implying that the collision of its component winds is not the principal source of diffuse X-rays. The sixfold or more difference in X-ray luminosity we see between Rosette and M17 is roughly consistent with

the difference in their O star populations (Rosette has two stars of type O6 or earlier; M17 has seven) and their wind kinetic energies (2×10^{48} ergs in Rosette; 9×10^{48} ergs in M17).

The Carina Nebula, where the diffuse soft X-ray luminosity is of order 10^{35} ergs s^{-1} , represents the first stages of starburst phenomena, where rich stellar clusters of a variety of ages have an enormous effect on their environment. Many powerful winds are colliding with each other, encountering the cloud edges, and quite possibly interacting with SNRs. The X-ray plasma is probably not relatively uniform with a simple laminar outward flow as we see in M17. Rather, motions are likely in multiple directions, with shocks, turbulence, and strong density inhomogeneities. Such a superheated, shock-dominated hot interstellar environment is seen in starburst superbubbles such as 30 Doradus (Chu & Mac Low 1990; Dennerl et al. 2001), the mild starburst nucleus in our Galactic center region (Wang, Gotthelf, & Lang 2002; Munro et al. 2003), and in true nuclear starbursts such as NGC 253 (Strickland et al. 2003) and M82 (Griffiths et al. 2000). In the latter case, the overpressure of the supernova- and wind-heated interstellar medium drives kiloparsec-scale winds of enriched material into the intergalactic medium.

A critical issue raised by these studies is the likely presence of a hard ($kT \sim 5$ keV, or 58 MK) as well as soft ($kT \simeq 0.8$ keV, or 9 MK) plasma in some portions of some H II regions. It is reported in RCW 38, NGC 3603, and the Arches cluster but not in W3 or the less rich stellar associations like the ONC or Rosette. In the intermediate case of M17, unresolved hard X-rays are spatially coincident with the highest concentrations of stars; a diffuse component cannot be distinguished from an unresolved component because of the large population of faint, embedded pre-main-sequence stars. In all these examples, we must be aware of the possible contamination by the population of low-mass embedded stars masquerading as diffuse gaseous emission; in regions with evolved stars or a range of cluster ages, contamination by SNRs must also be considered. If real, this diffuse hard component must represent a more efficient conversion of wind kinetic energy into plasma thermal energy. It may require nonlinear transport processes at the interface of the wind and molecular cloud as described by Dorland & Montmerle (1987).

One possibility for the eventual dissipation of the wind energy is that the plasma pressure overcomes the ambient pressure at a weak point, such as a low-density region at the periphery of a molecular cloud; this would be reminiscent of the “champagne flow” invoked for H II regions like Orion. This is probably the case for M17, which displays a clear flow of gas toward the boundary with the interstellar medium. Alternatively, the plasma may “leak” through fissures, simply flowing past denser regions; this might be the case for Rosette, although a flow nearly along the line of sight is also possible. In both cases, the gas then escapes into the surrounding low-pressure interstellar medium, adding to the network of worms and chimneys created in the Galactic disk by supernova explosions (de Avillez & Berry 2001).

If the surrounding medium is dense enough to hold the plasma, the wind energy must be efficiently dissipated at or near the periphery of the plasma bubble, since there appears to be little or no expansion of the H II shell. In the case of a steep density gradient (such that the slope is smaller than the mean free path of the plasma electrons in the H II

region), Dorland & Montmerle (1987) have shown that no Maxwellian electron velocity distribution is possible, and that a high-energy electron tail efficiently takes away the wind energy via nonlinear conduction. These nonthermal electrons, which would radiate hard X-rays, end up losing their energy unnoticed in the surrounding photodissociation region. This may be occurring around the embedded RCW 38 cluster, if the hard diffuse X-ray emission there is not due to a SNR and/or the embedded stellar population. Another possibility for wind energy dissipation is that the hot plasma directly evaporates the surrounding medium by photoevaporation resulting from the complete absorption of the (soft) X-ray photons and/or from heating by the bremsstrahlung keV electrons.

9. CONCLUDING COMMENTS

9.1. Summary of Findings

Chandra ACIS-I images of the Rosette and M17 H II regions in the 0.5–8 keV X-ray band reveal diffuse emission extending over several parsecs. Unlike studies with previous satellites, the high resolution of the *Chandra* mirrors and detectors and low detector noise allow faint diffuse emission to be studied in quantitative detail, even in the midst of hundreds of stellar X-ray sources. Strong arguments are presented that the emission is not attributable to SNRs or low-luminosity stellar sources. It is produced by plasma at $T \sim 1$ MK and ~ 10 MK with luminosities of $\leq 6 \times 10^{32}$ ergs s^{-1} in Rosette and 3.4×10^{33} ergs s^{-1} in M17. The emission has a roughly uniform, center-brightened appearance. In Rosette, the X-ray gas surrounds the ionizing cluster, filling the hole within the well-known ring of H α and radio continuum emission. In M17, the gas is roughly coincident (in projection) with the H α emission, brightest around the cluster core and flowing eastward for several parsecs.

9.2. Astrophysical Implications

We establish that only a small portion of the wind energy and a tiny fraction of the mass appears in the observed diffuse X-ray plasma. Although cooling into the H II component is possible, we suspect that most of the wind energy and mass of these blister H II regions flow without cooling into the low-density interstellar medium. In this case, the fate of deeply embedded winds where the stars are completely surrounded by dense molecular gas will be different than in these blister H II regions.

Together with other recent reports from *Chandra* and *XMM-Newton*, this is the first unambiguous detection of the windswept bubble that has long been predicted to arise from the thermalization of OB stellar winds. We estimate that $\sim 10\%$ of the wind kinetic energy is converted to X-ray-emitting plasma, although it is still not clear whether most of the dissipation occurs in wind-wind or wind-cloud shocks. We suspect that both types of shocks are present. The low-temperature spectral component suggests that some postshock gas is cooling, but most of the gas mass and most of the kinetic energy of the winds probably stay in the form of bulk flow. This is clearly seen in M17, where the X-ray emission flows from the core of the stellar cluster, away from the dense molecular cloud and toward low-density interstellar environments. The OB wind energy is not, at least in these two cases, principally dissipated in turbulent layers or mass loading close to the O stars.

For some regions (such as Rosette), the physical conditions of the 10^4 K gas may not be well-established, if the derived pressure can change by a factor of 100 with different reasonable assumptions for geometry, clumpiness, and filling factor; compare the models of Celnik (1985) and Tsivilev et al. (2002). Derived physical parameters can also change substantially if the stellar mass-loss rates change by factors of 3 or more when clumping due to turbulence is considered (Moffat & Robert 1994); this was illustrated by Dunne03 for the case of M17. Dunne03 also showed that the presence of strong magnetic fields may inhibit heat conduction, thus reducing the X-ray luminosity in M17 below the values predicted by the standard wind-blown bubble models.

New high-resolution optical and near-infrared images of the hydrogen-line structures in H II regions are showing a rich, subparsec filamentary structure in the photodissociation regions (Jiang et al. 2002). This may change our ideas about the interface between the inner ten million degree plasma and the outer ten thousand degree photodissociated gas, and hence about their possible exchanges of energy. The two media may well coexist in some fashion over a certain distance, a situation reminiscent of SNRs expanding into the interstellar medium. These considerations require that the classical “Strömgren sphere” paradigm be seriously revised to better account for the existence of stellar winds.

In fact, one of the potential implications of this finding may be the need to reformulate our language and overall conception of H II regions. In M17, the apparent outflow of X-ray gas from the NGC 6618 cluster away from the molecular cloud might be termed an “X-ray fountain” or “X-ray champagne flow,” in analogy to the champagne model of photoevaporation of dense gas by OB ultraviolet radiation (Tenorio-Tagle 1979). For H II regions where most of the interior volume is filled with an X-ray-emitting plasma, as in M17 and Rosette, the cooler ionized gas responsible for H α and radio continuum emission is confined to a relatively thin layer near the boundary with the molecular cloud. Thus, the phrase “Strömgren sphere” might be replaced with “Strömgren shell” or “Strömgren surface.” For M17, this idea is supported by a recent high-resolution *JHK* image where the hydrogen-line emission is mostly concentrated in filaments and a thin “silver lining” around the dark cloud.¹⁴

The current sample of HMSFRs studied with modern X-ray instrumentation shows a large range of diffuse-emission properties, with reports of both hard and soft, bright and faint emission and spatial scales of fractions of a pc² to thousands of pc². Generally, nearby, less-obscured regions show soft, faint diffuse emission filling moderate-sized, presumably wind-blown, bubbles. More distant, obscured regions ionized by more early stars may sometimes exhibit hard diffuse emission, but the contribution of low-mass stellar sources is difficult to untangle. The soft component may be present but is probably absorbed. The specific character of diffuse X-rays in HMSFRs is governed by the details of star formation and the distribution of molecular material associated with each region.

In addition to clarifying H II region astrophysics, establishing the effects of OB winds on their environment is relevant for understanding the energetics of the interstellar

medium on a galactic scale. Stellar wind bubbles within an H II region can affect the evolution of later SNRs and superbubbles (Oey, Clarke, & Massey 2001). The integrated mechanical input of stellar winds generally exceeds that of SNRs over the full lifetime of a starburst event and, if efficient thermalization occurs, winds and supernovae together can power galactic superwinds (Leitherer, Robert, & Drissen 1992).

9.3. Prospects for Further Study

Chandra study of H II regions containing a variety of ionizing stellar clusters, with different wind sources and ages and in different gaseous environments, is likely to give additional insights into the fate of OB winds. We suspect that X-ray plasma will be commonly found in H II regions when several O stars with sufficiently strong winds are present. A deeper *Chandra* observation of the Rosette Nebula is planned, both to improve the discrimination between diffuse gas and the low-mass stellar population and to search for subtle gradients in the gas properties. For example, spectral or brightness changes in the X-ray emission around the molecular gas would show the wind termination shock (see § 7), while bright X-ray arcs between the principal O stars would reveal a wind-wind collision shock. The wind-cloud versus wind-wind heating mechanisms can also be tested by comparing the diffuse X-ray emission in embedded clusters to those that have largely evacuated cold gas from their environment.

Study of the optical line emission from these H II regions specifically to elucidate the windswept bubble model would also be helpful. High-resolution imaging may confirm that the line emission is confined to a shell around the photodissociation region and does not permeate the entire volume around the ionizing cluster. Optical line spectroscopy can investigate high-velocity components in the H II region, such as knots with $\simeq 100$ km s⁻¹ velocities reported by Meaburn & Clayton (1987) in M17 and by Clayton et al. (1998) in Rosette, to study the dynamical influence of the winds on the cooler gas.

While hot windswept bubbles in H II regions have been extensively modeled for several decades, most of these studies do not make specific predictions of X-ray luminosities, temperatures, and morphologies. Notable exceptions are the studies by Dorland & Montmerle (1987), Comerón (1997), and Cantó et al. (2000). These models are beginning to be revisited in light of the new *Chandra* findings (Stevens & Hartwell 2003). We suspect, for example, that winds with heavy mass loading or thick turbulent mixing layers are incompatible with our results while winds with strong shocks are favored, but Stevens & Hartwell (2003) favor mass loading from the disks of pre-main-sequence stars to explain the luminosity and temperature of Rosette. It would also be desirable to construct numerical three-dimensional hydrodynamic calculations with the specific configuration of wind sources and cold gaseous boundaries present in Rosette and M17. Comparing the predicted X-ray properties to our observations should give new insights into the structure (e.g., wind-wind vs. wind-cloud) and physics of the shocks that heat H II regions to X-ray temperatures.

Support for this effort was provided by *Chandra X-Ray Observatory* grant G01-2008X and by NASA contract NAS8-38252. E. D. F. thanks CEA/Saclay for hospitality

¹⁴ See <http://www.pparc.ac.uk/Nw/Press/uist.asp>.

during the study period. This research has made use of NASA's Astrophysics Data System and the SIMBAD database, operated at CDS, Strasbourg, France. We appreciate the insight gained through conversations with A. Dalgarno, K. Getman, C. Grant, M. Mac Low, C. McKee, J. Raymond, and C. Sarazin. We thank R. Chini for supplying

data and our referee, N. Miller, for his time and helpful comments, which improved the quality of this paper. This study was a true collaboration, with equal contributions made by the first three authors in the development of the paper and substantial supporting roles played by the other authors. L. K. T. is most grateful for this ensemble effort.

APPENDIX A

MASSIVE STARS IN M17 AND ROSETTE

Tables 5 and 6 give properties of the O and early B stars (through B3) in NGC 6618, the cluster exciting M17, and NGC 2244, the cluster exciting the Rosette Nebula, respectively. The tables are ordered by spectral type. All values are obtained from the literature except for the final column, which indicates whether the star is detected in our *Chandra* ACIS images. There may be additional early-type members of NGC 6618; visual studies of this cluster are complicated by heavy obscuration and confusion with the bright H II region and near-infrared studies have not covered the entire cluster, which may extend up to 25' (~ 11.6 pc) in diameter (Pérez 1991). In Rosette, the census of early stars is probably more complete because the cluster core is less absorbed. Some of the stars listed in Table 6, however, lie well outside the cluster coronal radius of 7.95 pc (~ 19.5) measured by Nilakshi et al. (2002) and thus may not be members of NGC 2244. They may be associated with other star-forming regions in the Mon OB2 association or the RMC, since they possess other properties that are consistent with NGC 2244 cluster membership (Kuznetsov et al. 2000).

TABLE 5
O AND EARLY B STARS IN NGC 6618 (M17 CLUSTER)

NAME ^a			R.A. (J2000.0) ^b	DECL. (J2000.0) ^b	SPECTRAL TYPE ^c	ACIS DETECTED?
CEN	B	OI				
37	174	...	18 20 30.54	-16 10 53.3	O3-O6	Yes
43	137	...	18 20 33.14	-16 11 21.6	O3-O4	Yes
1	189	341	18 20 29.92	-16 10 45.5	O4+O4 ^d	Yes
102	305	780	18 20 23.05	-16 07 58.9	O5	No
2	111	337	18 20 34.55	-16 10 12.1	O5	Yes
...	...	345	18 20 27.52	-16 13 31.8	O6	Yes
18	260	326	18 20 25.94	-16 08 32.3	O7-O8	Yes
25	164	...	18 20 30.92	-16 10 08.0	O7-O8	Yes
34	358	715	18 20 21.48	-16 10 00.0	O8	No
16	311	258	18 20 22.76	-16 08 34.3	O9-B2	Yes
61	181	...	18 20 30.30	-16 10 35.2	O9-B2	Yes
3 ^e	98	342	18 20 35.47	-16 10 48.9	O9	Yes
31	289	...	18 20 24.45	-16 08 43.3	O9.5	Yes
51	243	...	18 20 26.64	-16 10 03.7	Early B	No ^f
92	331	770	18 20 21.77	-16 11 18.3	B0	No
28	150	...	18 20 31.92	-16 11 38.6	B0	Yes
57	269	736	18 20 25.59	-16 11 16.3	B1	Yes
95	266	773	18 20 25.72	-16 08 59.1	B1	No
101	206	779	18 20 29.04	-16 11 10.5	B1	Yes
97	204	775	18 20 29.31	-16 09 43.3	B1	Yes
100	159	778	18 20 31.25	-16 09 29.9	B1	Yes
45	18 20 35.6	-16 10 53	B1	No
33	324	714	18 20 22.19	-16 09 19.5	B2	No
24	275	...	18 20 25.11	-16 10 26.7	B2	No
49	268	...	18 20 25.35	-16 10 19.2	B2	No
48	248	...	18 20 26.31	-16 10 16.4	B2	No
90	241	768	18 20 26.91	-16 10 58.8	B2	Yes
85	223	763	18 20 28.29	-16 10 49.8	B2	Yes
84	207	762	18 20 29.01	-16 10 42.5	B2	No
96	...	774	18 20 29.2	-16 09 39	B2	No
89	190	767	18 20 29.88	-16 10 11.5	B2	No
99	152	777	18 20 31.83	-16 09 46.2	B2	Yes
17	336	269	18 20 21.40	-16 11 40.7	B3	Yes
93	337	771	18 20 21.43	-16 10 41.2	B3	Yes
35	333	716	18 20 21.54	-16 09 39.4	B3	Yes

TABLE 5—Continued

NAME ^a			R.A. (J2000.0) ^b	DECL. (J2000.0) ^b	SPECTRAL TYPE ^c	ACIS DETECTED?
CEN	B	OI				
75	308	754	18 20 22.98	−16 08 14.8	B3	No
94	299	772	18 20 23.76	−16 10 35.8	B3	No
91	282	769	18 20 24.76	−16 11 09.0	B3	Yes
83	267	761	18 20 25.63	−16 10 54.1	B3	Yes
14	254	703	18 20 26.09	−16 10 51.5	B3	No
26	253	...	18 20 26.13	−16 11 05.1	B3	Yes
74	245	753	18 20 26.77	−16 08 22.9	B3	No
46	230	726	18 20 27.89	−16 11 02.5	B3	Yes
47	227	727	18 20 28.07	−16 11 09.3	B3	No
65	220	744	18 20 28.32	−16 09 58.5	B3	No
27	197	708	18 20 29.93	−16 11 37.6	B3	Yes
44	18 20 30.4	−16 10 05	B3	No
50 ^g	...	730	18 20 26.35	−16 10 19.0	B3	No
58 ^g	18 20 22.45	−16 10 17.3	B3	No
81 ^h	B3	...
82 ^g	...	760	18 20 25.56	−16 10 55.1	B3	Yes

^a CEN = Chini et al. 1980; B = Hanson et al. 1997, derived from Bumgardner 1992; OI = Ogura & Ishida 1976.

^b Positions are from Hanson et al. 1997, Chini & Wargau 1998, or SIMBAD.

^c Spectral types from Hanson et al. 1997 or Chini et al. 1980; assumed to be luminosity class V.

^d The O4-O4 binary Kleinmann's Anonymous Star; see § 2.1.

^e BD −16°4818.

^f Source lies in gap between ACIS CCD chips.

^g Positions provided by R. Chini 2003, private communication.

^h Position unavailable, so no X-ray match can be made.

TABLE 6
O AND EARLY B STARS IN NGC 2244 (ROSETTE CLUSTER)

NAME ^a			R.A. (J2000.0) ^b	DECL. (J2000.0) ^b	SPECTRAL TYPE ^c	ACIS DETECTED?
HD/BD	J	OI				
46223	3	203	06 32 09.32	+04 49 24.9	O4 V((f)) [∞]	Yes
46150	2	122	06 31 55.53	+04 56 34.5	O5 V((f)) [∞]	Yes
46485	...	387	06 33 50.96▷◁	+04 31 31.6▷◁	O7 V [∞]	Yes ^e
46056	7	84	06 31 20.88	+04 50 04.0	O8 V((f))	Yes
46149	4	114	06 31 52.54	+05 01 59.4	O8.5 V((f))	Yes
258691	...	376	06 30 33.33	+04 41 27.9	O9 V((f))	Not in FOV
46202	6	180	06 32 10.48	+04 58 00.1	O9 V((f))	Yes
259238	19	239	06 32 18.21 [∞]	+05 03 21.7 [∞]	B0 V [∞]	Not in FOV
46106	5	115	06 31 38.40	+05 01 36.6	B0.2 V	Yes
*	06 31 37.10	+04 45 53.7	B0.5 V	Not in FOV
259135†	8	200	06 32 00.62	+04 52 41.1	B0.5 V ^d	Yes
* [♠]	06 33 37.51	+04 48 47.0	B0.5 V	Not in FOV
259012	9A	80	06 31 33.48	+04 50 40.0	B1 V	Yes
259105	10	128	06 31 52.02	+04 55 57.5	B1 V	No
+04°1299s	11	201	06 32 06.15	+04 52 15.6	B1 III	Yes
46484	...	389	06 33 54.41▷◁	+04 39 44.6▷◁	B1 V [∞]	Not in FOV
+05°1281B	14	193	06 31 58.95	+04 55 40.1	B1.5 V	Yes
259172	16	167	06 32 02.59	+05 05 08.9	B2 V	Not in FOV
...	...	345	06 33 06.58 [∞]	+05 06 03.4 [∞]	B2 [□]	Not in FOV
+04°1295p	15	79	06 31 31.48	+04 51 00.0	B2.5 V	No
...	27	130	06 31 47.90	+04 54 18.3	B2.5 V [∞]	No
...	23	190	06 31 58.92 [∞]	+04 56 16.1 [∞]	B2.5 V _n [∞]	No
...	22	172	06 32 09.9△	+05 02 14△	B2.5 V [∞]	No
*	...	274	06 32 24.24	+04 47 04.0	B2.5 V	No ^f
*	...	392	06 33 50.56	+05 01 37.8	B2.5 V	Not in FOV
...	33	194	06 32 15.48	+04 55 20.2	B3 [□]	Yes
*	06 32 22.49	+04 55 34.4	B3 V	Yes

TABLE 6—Continued

NAME ^a			R.A. (J2000.0) ^b	DECL. (J2000.0) ^b	SPECTRAL TYPE ^c	ACIS DETECTED?
HD/BD	J	OI				
259268	20	241	06 32 23.05◊	+05 02 45.7◊	B3□	Not in FOV
259300	17	253	06 32 29.40	+04 56 56.3	B3 Vp◊	Yes
...	...	334	06 32 51.79◊	+04 47 16.1◊	B3□	Yes ^f
*	06 33 10.16	+04 59 50.2	B3 V	Not in FOV

^a J = Johnson 1962; OI = Ogura & Ishida 1981; asterisk (*) = Massey, Johnson, & DeGioia-Eastwood 1995; dagger (†) = V578 Mon; spade (♠) = IRAS 06309+0450.

^b Positions from Massey et al. 1995, except those marked with a bowtie (⋈) from *Hipparcos*, a diamond (◊) from Ogura & Ishida 1981, and a triangle (△) from Park & Sung 2002.

^c Spectral types from Massey et al. 1995, except those marked with a heart (♥) from Walborn et al. 2002, a diamond (◊) from Ogura & Ishida 1981, and a square (□) from Kuznetsov et al. 2000.

^d Double star.

^e Observed in Rosette Field 4.

^f Observed in Rosette Field 2.

APPENDIX B

ACIS DATA REDUCTION PROCEDURE

Our ACIS data reduction begins with the Level 1 event list (“*evt1* file”) and associated files (e.g., the telescope aspect solution, contained in the “*asol1*” file). We require Level 1 data products because they contain information that is unavailable in the more highly processed Level 2 files. Many of the diagnostic plots described below are easily generated by “*Event Browser*,” part of the “Tools for ACIS Review and Analysis” (TARA) package developed by P. Broos and other members of the ACIS team and available to all interested users.¹⁵

The first step is to improve the absolute astrometry of the field by registering X-ray point sources with (typically) visual catalogs of high astrometric precision. If enough matches are found in the field, we use the Tycho 2 catalog of *Hipparcos* positions (Høg et al. 2000). If the field contains few Tycho matches (as is the case for M17), we can usually obtain enough matches with the USNO-A2.0 catalog (see footnote 7 above) to improve the positions. Preliminary *Chandra* source positions are obtained by running *wavdetect* (Freeman et al. 2002) on a Level 2 event list, including only the central part of the ACIS-I array for speed and because the small PSFs in this region will yield better X-ray positions. We then compute the median offset between X-ray and visual positions in right ascension and declination separately, discarding outliers that are likely due to mismatched sources. The astrometry of the observation is adjusted by offsetting the right ascension and declination columns in the aspect file, offsetting the nominal pointing coordinates, and reprojecting the event data.

We remove the pixel randomization when the events are reprojected; in our experience, any observation longer than a few ks samples enough pixels due to spacecraft dither that any pixel-to-pixel gain variations are already averaged out, and the best possible positions and sharpest PSFs are critical here, to enable source matching with catalogs from other wavebands. Note that the sky coordinates (x, y) of the events will not change (except for the removal of the pixel randomization); reprojection simply moves the x/y system on the sky (in both *asol1* and *evt1* files). A comparison of the old and new positions is made by examining the distribution of the distance each event moved. The pixel randomization consists of uniform random numbers $[-0.5, 0.5]$ added to the CCD chip coordinates. With a nonzero roll angle, the randomization in x/y coordinates is not a uniform distribution, but it should have a characteristic shape, with a maximum value of $(0.5^2 + 0.5^2)^{1/2} = 0.7$ pixels.

The data are then examined for possible processing errors. The set of flight event grades [24, 66, 107, 214, 255] are removed in the on-board processing (they are not telemetered to the ground). Thus, the appearance of many events with these grades in the Level 1 data strongly suggests a processing error, such as the use of an incorrect bias. If the field contains a very bright source, then we have the opportunity to look for a variety of problems in the aspect solution. By plotting event x and y positions versus event arrival time for a small region around the brightest source, we can look for “movement” of the source across the sky. Incomplete dedithering might produce periodic movement; aspect camera problems might produce jumps in the position; motion of the Science Instrument Module at the beginning or end of the observation will make the source appear to run off the field completely.

If the data were obtained in “Timed Event, Very Faint” mode, each event consists of a 5 pixel \times 5 pixel event island. Code was developed by A. Vikhlinin (CXC)¹⁶ to use the outer pixels in this island as a way to reduce background. This routine sets a status bit that flags events with high outer pixels. It will flag good events from bright sources as well as bad events, so it must be used with caution. For appropriate data, this routine is applied at this stage of the processing and the event list is filtered to remove flagged events. As with all filtering steps, we carefully examine the events that are discarded to make sure that the filtering was appropriate and was applied correctly.

¹⁵ See <http://www.astro.psu.edu/xray/docs/TARA>.

¹⁶ See http://hea-www.harvard.edu/~alexey/vf_bg/vfbg.html.

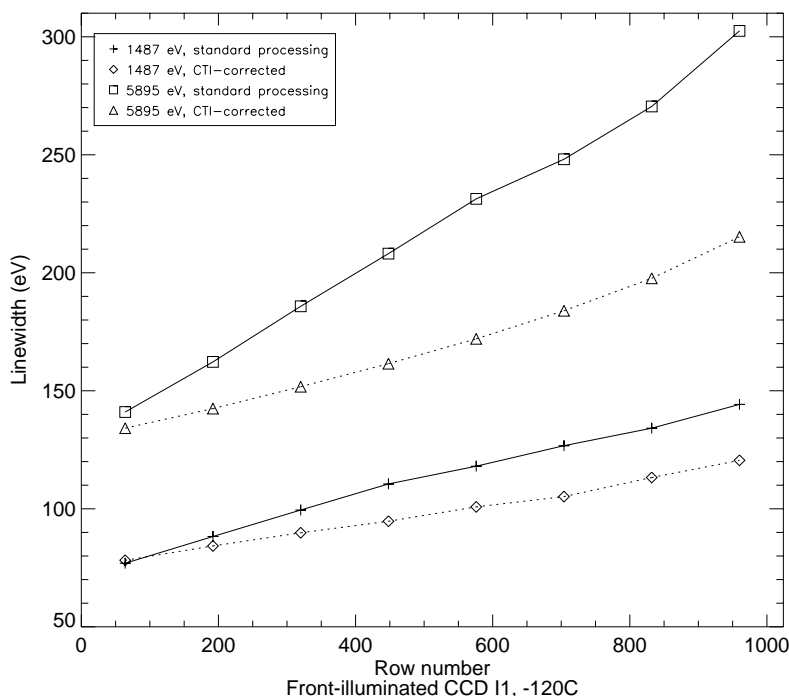


FIG. 10.—ACIS spectral resolution on an FI CCD as a function of row number, before and after CTI correction using the Penn State algorithm. By reducing the spectral resolution variation across the CCDs, CTI correction substantially improves spectral analysis of diffuse structures on ACIS-I.

The data are then corrected for radiation-induced CTI using the method developed at Penn State (Townsend et al. 2002b). Correcting for CTI improves spectral resolution of extended sources by $\sim 20\%$ – 40% . This is illustrated in Figure 10, which gives the energy resolution of ACIS-I CCDs as a function of CCD row number both before and after CTI correction, shown using the FWHM of the Al $K\alpha$ and Mn $K\alpha$ calibration lines in the ACIS External Calibration Source (ECS; Townsend et al. 2002a).

The latest release of CIAO (2002 November; ver. 2.3) now includes a CTI corrector for front-illuminated (FI) CCDs, developed by the MIT ACIS group and the CXC. It employs the same forward-modeling approach used in the Penn State corrector, although the implementation and details of the model are different. This code was not available when the M17 and Rosette data were analyzed and does not apply to back-illuminated (BI) devices, so the Penn State corrector was used; which code we use in the future will depend on performance, as assessed by CTI correction of the ACIS ECS data. These calibration observations are made every orbit, as a way to monitor CTI and other aspects of ACIS performance. They can be used as a check on the uniformity of the energy calibration across the field and are available via the Provisional Data Retrieval Interface.¹⁷ The CXC can provide users with the observation identification number (“obsid”) of the calibration observations most appropriate for a given celestial observation.

To check the Penn State CTI corrector performance on the M17 data, we ran the corrector on the closest ECS data, observation ID 61277. A plot of CHIPY versus energy showed that the corrector still worked well for improving spectral resolution; it was tuned using data from 2000 January through 2001 January, so it was prudent to check its performance for the M17 data, which were obtained in 2002 March. This test did reveal a problem, however: the corrector was not doing a good job of regularizing the gain across the CCD, so the event energies showed a clear decline of $\sim 1\%$ from the bottom of the CCD to the top. This test motivated us to include the time dependence of the CTI as measured by C. Grant¹⁸ in the Penn State CTI corrector. This new code restored the flat gain across the CCDs for this observation; in fact, this time-dependent corrector surpasses the original corrector for *all* ACIS observations made at a focal plane temperature of -120°C , for both FI and BI devices. Analysis products developed for use with the original Penn State CTI corrector (RMF and QEU files) are still valid for the time-dependent corrector; these products and the corrector code are available on-line.¹⁹

The events are then filtered in various ways. The standard grade filter (retaining only *ASCA*-type grades 0, 2, 3, 4, and 6) is applied and events with bad grades are examined to make sure that they are truly bad (for example, legitimate X-ray point sources might show up in an image made of the bad grades; this would be an indication of photon pileup in these sources and a warning to the user that these sources must be analyzed more carefully). The Level 1 event lists include a “status” column containing 32 single-bit flags representing various reasons why an event may be deemed undesirable.²⁰ Most observers will want to respect most of these flags, removing events that have a flag value of 1. There is one notable exception: bits 16–19 are

¹⁷ See <http://cxc.harvard.edu/cgi-gen/cda/retrieve5.pl>.

¹⁸ See <http://space.mit.edu/~cgrant/cti/cti120.html>.

¹⁹ See <http://www.astro.psu.edu/users/townsend/cti>.

²⁰ See http://cxc.harvard.edu/ciao2.2.1/data_products_guide/acis_status_bits.html for the definitions of these flags.

set by the pipeline tool *acis_detect_afterglow* in an attempt to identify spurious events due to cosmic-ray afterglows (“flaring pixels”). This tool suffers the problem of flagging real events from even moderately bright sources.²¹ By simply applying a [status = 0] filter or by using the Level 2 event list, significant numbers of legitimate events from point sources will be discarded. Again, this behavior is not restricted to bright point sources. To avoid this problem, at this stage of the processing we follow the uncontroversial status flags but ignore flags 16–19 by applying this filter: [status = 000000000000xxxx00000000000000000].

The CXC distributes a “flight timeline” (flt1.fits) file containing good time interval (GTI) tables that designate certain time intervals deemed “bad” by the CXC pipelines. We do not know exactly what criteria are used by the CXC to determine these GTIs, but many observations contain small gaps in the aspect solution that are recorded in the flight timeline. Filtering with these GTI tables is applied as part of the Level 2 processing, and we apply it here. We search for additional aspect glitches by examining the *acis.asol1* file, a time series of the absolute pointing (right ascension, declination, roll angle).

Because of solar activity, the particle background can increase substantially over short timescales. We search for these background flares, which are especially troublesome on BI CCDs, by examining light curves from each CCD using the CXC’s *lightcurve* tool. We then modify the GTI files and apply them to the event list to exclude times containing flares. We always verify that the cleaned data no longer show flares by recomputing the light curves.

The data are then searched for hot columns or hot pixels that are not removed by the standard processing. These can be found by careful examination of each CCD (in chip coordinates); the image must retain 1 pixel binning in order to see the hot columns. Another good way to find hot columns is to make a histogram of events as a function of the CHIPX coordinate; columns with too many events are then easily noticed. It is important to check the energies at which these bad columns go away. We have found that most are gone above 0.7 keV, virtually all are gone above 1 keV, and absolutely all are gone above 2 keV. The worst CCD by far is the noisy CCD8 (S4). We find that we almost always have to filter CCD0 (I0), column 3, to remove events below 700 eV. Also, there is a hot pixel in CCD6 (S2), at chip coordinates (766, 501). Note that any spatial filtering done here is *not* reflected in the bad pixel file and is thus not accounted for in ARF or exposure map calculations. For making smoothed images, it is better to remove the bad columns and suffer an imperfect exposure map than to leave them in, especially if soft extended emission might be present or there are other reasons to work in very soft bands (<1 keV).

CIAO provides the command *acisreadcorr* to remove readout streaks due to bright sources.²² We do not use it in this recipe, however, because we are mainly concerned with large fields full of point sources. In these fields, it is highly likely that other point sources fall under the readout streak of the bright one. The *acisreadcorr* operation removes *all* the events in the streak and replaces them with artificial data according to some spectral shape of the nominal background that the user provides.

This filtered event list is then examined to make sure that it still contains a GTI table for each CCD and that appropriate FITS header keywords are present and set to the right values. A very coarse energy filter is then applied to remove events that we know are background. These energy limits (0–10.5 keV) are well outside the range that will be used for spectral fitting. This needs to be done here even if it was done before CTI correction, because the corrector moves some events up to very high energies when it corrects cosmic rays.

Note that these data still have flaring pixels in them, because applying the flaring pixel filter removes good events. These data have not been band-limited (filtered strongly by energy or pulse-height invariant [PI] bins). Further filtering by energy is useful when making images and for timing analysis, but must not be done for spectral analysis because the low and high energy ranges specified will, in general, fall in the middle of PI or pulse-height amplitude (PHA) bins, which are used to construct spectra. Generally speaking, the user should specify the energy range over which spectra will be fitted directly in the fitting package, rather than by band-limiting the data. The flaring pixel filter and an energy filter to minimize background are applied before source-searching is done.

APPENDIX C

AN ALTERNATIVE METHOD FOR ADAPTIVE-KERNEL IMAGE SMOOTHING

The smoothed images shown in Figures 4 and 7 were constructed using a simple adaptive kernel smoothing method. The smoothing kernels consist of the null kernel

$$k(0, i, j) = \delta(i, j) = \begin{cases} 1, & i = 0, j = 0, \\ 0, & \text{otherwise,} \end{cases}$$

which produces no smoothing, plus a family of two-dimensional Gaussians with integer sigma values $r = \{1, 2, 3, \dots\}$,

$$k(r, i, j) = \exp\left(-\frac{i^2 + j^2}{2r^2}\right).$$

²¹ See http://cxc.harvard.edu/ciao2.2.1/caveats/acis_cray.html for an explanation of this problem.

²² See <http://asc.harvard.edu/ciao/ahelp/acisreadcorr.html>.

For a particular kernel size $r = R$, the flux at position (X, Y) is estimated as

$$\text{flux}(X, Y) = \frac{\text{counts}}{\text{exposure}}, \quad (1)$$

where

$$\begin{aligned} \text{counts} &= \sum_{x \in \text{Obs}} \sum_{y \in \text{Obs}} k(R, x - X, y - Y) \text{image}(x, y), \\ \text{exposure} &= \sum_{x \in \text{Obs}} \sum_{y \in \text{Obs}} k(R, x - X, y - Y) \text{emap}(x, y). \end{aligned}$$

“Obs” is the set of pixels in the “observed” region (positive exposure) of the scene, “image” is the integer-valued image of observed counts, and “emap” is the exposure map.

To derive an estimate of the error on the flux value, we first note that each pixel in our observed counts image, $\text{image}(x, y)$, is of course a sample from an unknown underlying Poisson distribution associated with that pixel. We make the simplifying assumption that all the pixels under the kernel have the *same* true flux (which we just estimated). By multiplying that flux by the pixel’s exposure value, we then compute the mean number of counts that should be observed in each pixel if the image was repeatedly observed:

$$\text{mean}(x, y) = \text{flux}(X, Y) \text{emap}(x, y).$$

Each pixel’s (Poisson) variance is assumed to be that mean value. We then propagate the variances of the distributions through the linear equation (1) in the usual way to obtain an error for our flux estimate:

$$\text{error} = \frac{\sqrt{\sum_{x \in \text{Obs}} \sum_{y \in \text{Obs}} [k(R, x - X, y - Y)]^2 \text{flux}(X, Y) \text{emap}(x, y)}}{\text{exposure}}.$$

The flux and flux error are used to define a simple “significance” value,

$$\begin{aligned} \text{significance} &= \frac{\text{flux}}{\text{error}} \\ &= \frac{\sum_{x \in \text{Obs}} \sum_{y \in \text{Obs}} k(R, x - X, y - Y) \text{image}(x, y)}{\sqrt{\sum_{x \in \text{Obs}} \sum_{y \in \text{Obs}} [k(R, x - X, y - Y)]^2 \text{flux}(X, Y) \text{emap}(x, y)}}, \end{aligned}$$

which increases as r increases since more counts are encompassed under the kernel. The observer supplies a significance threshold, and at each position (X, Y) the flux is estimated using the smallest kernel size, r , that produces a significance exceeding the threshold. Thus, regions of low flux are more heavily smoothed than regions of higher flux. The significance threshold controls the overall level of smoothing. A map of the kernel sizes chosen is returned by the smoothing program.

Application of the kernel to the exposure map in equation (1) is required for accurate smoothing of any wide-field ACIS image because the exposure varies significantly due to chip gaps and bad regions of the detector, as shown in the example swiss-cheese exposure map in Figure 11. The algorithm naturally handles unobserved regions, such as areas explicitly masked by the observer and areas outside the FOV of ACIS, because those zero-count and zero-exposure pixels do not affect either the flux or flux error computations. As you would expect, an unobserved region tends to cause neighboring observed regions to be more heavily smoothed since a larger kernel must be used to find an adequate number of counts. Note that the algorithm will estimate a flux for unobserved pixels (zero exposure) using the nearby observed regions, as in Figures 4d and 7d. This is of course a form of interpolation.

The smoothing program recognizes a negative value in the exposure map as a flag specifying that the position is “off-field,” meaning that no flux estimate should be computed there. We flag unobserved pixels in this way for several purposes: (1) Pixels outside the FOV of ACIS represent regions of the sky totally unobserved. Estimates of the sky flux on those regions are inappropriate since they would be extrapolations. It is desirable to include in this off-field category pixels at the edge of the detector that have very small exposure (due to dithering) because normalization by very small exposure values leads to noisy results. The off-field category can be most easily defined by simply thresholding the original exposure map (prior to application of the swiss-cheese mask regions). (2) In Figures 4b and 7b, we flagged as off-field all the pixels that were masked by the observer, preventing any interpolation over the holes. (3) In Figures 4c and 7c, we flagged as off-field those masked pixels that were more than a certain distance from any on-field pixel. This compromise approach fills in many small holes that are distracting to the eye, while avoiding making gross interpolations across large masked regions.

This algorithm has been implemented as the IDL program *adaptive_density_2d.pro* and is part of the publicly available TARA software package mentioned in Appendix B.

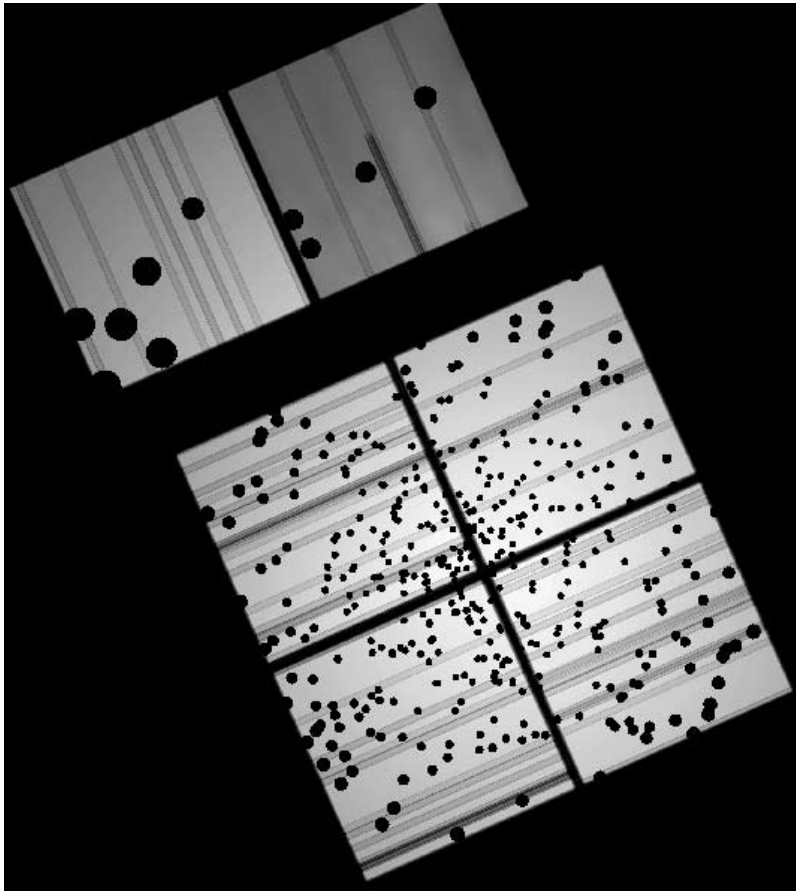


FIG. 11.—Example ACIS-I exposure map, including the swiss-cheese masks

REFERENCES

- Abbott, D. C. 1982, *ApJ*, 263, 723
- Aller, L. H. 1956, *Gaseous Nebulae* (London: Chapman & Hall)
- Ando, M., Nagata, T., Sato, S., Mizuno, N., Mizuno, A., Kawai, T., Nakaya, H., & Glass, I. S. 2002, *ApJ*, 574, 187
- Arnaud, K. A. 1996, in *ASP Conf. Ser. 101, Astronomical Data Analysis Software and Systems V*, ed. G. H. Jacoby & J. Barnes (San Francisco: ASP), 17
- Arthur, S. J., Dyson, J. E., & Hartquist, T. W. 1993, *MNRAS*, 261, 425
- Bally, J., Feigelson, E. D., & Reipurth, B. 2003, *ApJ*, 584, 843
- Berghöfer, T. W., & Christian, D. J. 2002, *A&A*, 384, 890
- Brinkman, A. C., et al. 2001, *A&A*, 365, L324
- Brogan, C. L., & Troland, T. H. 2001, *ApJ*, 560, 821
- Bumgardner, T. E. 1992, M.S. thesis, Ohio State Univ.
- Cantó, J., Raga, A. C., & Rodríguez, L. F. 2000, *ApJ*, 536, 896
- Capriotti, E. R., & Kozminski, J. F. 2001, *PASP*, 113, 677
- Celnik, W. E. 1985, *A&A*, 144, 171
- . 1986, *A&A*, 160, 287
- Chartas, G., Brandt, W. N., Gallagher, S. C., & Garmire, G. P. 2002, *ApJ*, 579, 169
- Chini, R., Elsässer, H., & Neckel, T. 1980, *A&A*, 91, 186
- Chini, R., Nielbock, M., & Beck, R. 2000, *A&A*, 357, L33
- Chini, R., & Wargau, W. F. 1998, *A&A*, 329, 161
- Chu, Y., Guerrero, M. A., & Gruendl, R. A. 2003, in *IAU Symp. 209, Planetary Nebulae: Their Evolution and Role in the Universe* (San Francisco: ASP), in press
- Chu, Y., & Mac Low, M. 1990, *ApJ*, 365, 510
- Chu, Y.-H. 2003, in *IAU Symp. 212, A Massive Star Odyssey: From Main Sequence to Supernova*, ed. K. A. van der Hucht et al. (San Francisco: ASP), in press
- Chu, Y.-H., Gruendl, R. A., & Guerrero, M. A. 2003, *Rev. Mexicana Astron. Astrofis. Ser. Conf.*, 15, 62
- Clayton, C. A., Ivchenko, V. N., Meaburn, J., & Walsh, J. R. 1985, *MNRAS*, 216, 761
- Clayton, C. A., Meaburn, J., Lopez, J. A., Christopoulou, P. E., & Goudis, C. D. 1998, *A&A*, 334, 264
- Comerón, F. 1997, *A&A*, 326, 1195
- Cox, P., Deharveng, L., & Leene, A. 1990, *A&A*, 230, 181
- de Avillez, M. A., & Berry, D. L. 2001, *MNRAS*, 328, 708
- Dennerl, K., et al. 2001, *A&A*, 365, L202
- Dorland, H., & Montmerle, T. 1987, *A&A*, 177, 243
- Dorland, H., Montmerle, T., & Doom, C. 1986, *A&A*, 160, 1
- Dunne, B. C., Chen, C.-H., Lowry, J. D., Townsley, L. K., Gruendl, R. A., Guerrero, M. A., & Chu, Y.-H. 2003, *ApJ*, 590, 306 (Dunne03)
- Dyson, J. E. 1977, *A&A*, 59, 161
- Dyson, J. E., & de Vries, J. 1972, *A&A*, 20, 223
- Dyson, J. E., Williams, R. J. R., & Redman, M. P. 1995, *MNRAS*, 277, 700
- Ebisawa, K., Maeda, Y., Kaneda, H., & Yamauchi, S. 2001, *Science*, 293, 1633
- Evans, N. R., Seward, F. D., Krauss, M. I., Isobe, T., Nichols, J., Schlegel, E. M., & Wolk, S. J. 2003, *ApJ*, 589, 509
- Favata, F., Fridlund, C. V. M., Micela, G., Sciortino, S., & Kaas, A. A. 2002, *A&A*, 386, 204
- Feigelson, E. D. 2001, in *ASP Conf. Ser. 234, X-Ray Astronomy 2000*, ed. R. Giacconi, S. Serio, & L. Stella (San Francisco: ASP), 131
- Feigelson, E. D., Broos, P., Gaffney, J. A., Garmire, G., Hillenbrand, L. A., Pravdo, S. H., Townsley, L., & Tsuboi, Y. 2002, *ApJ*, 574, 258
- Felli, M., Massi, M., & Churchwell, E. 1984, *A&A*, 136, 53
- Flaccomio, E., Damiani, F., Micela, G., Sciortino, S., Harnden, F. R., Murray, S. S., & Wolk, S. J. 2003, *ApJ*, 582, 382
- Fountain, W. F., Gary, G. A., & Odell, C. R. 1979, *ApJ*, 229, 971
- Freeman, P. E., Kashyap, V., Rosner, R., & Lamb, D. Q. 2002, *ApJS*, 138, 185
- García, B., & Mermilliod, J. C. 2001, *A&A*, 368, 122
- Getman, K. V., Feigelson, E. D., Townsley, L., Bally, J., Lada, C. J., & Reipurth, B. 2002, *ApJ*, 575, 354
- Glushkov, Y. I. 1998, *Astron. Rep.*, 42, 137
- Gregorio-Hetem, J., Montmerle, T., Casanova, S., & Feigelson, E. D. 1998, *A&A*, 331, 193
- Griffiths, R. E., Ptak, A., Feigelson, E. D., Garmire, G., Townsley, L., Brandt, W. N., Sambruna, R., & Bregman, J. N. 2000, *Science*, 290, 1325
- Hanson, M. M., Howarth, I. D., & Conti, P. S. 1997, *ApJ*, 489, 698
- Henning, T., Klein, R., Launhardt, R., Lemke, D., & Pfau, W. 1998, *A&A*, 332, 1035
- Hensberge, H., Pavlovski, K., & Verschueren, W. 2000, *A&A*, 358, 553
- Hillenbrand, L. A. 1997, *AJ*, 113, 1733
- Hillenbrand, L. A., Massey, P., Strom, S. E., & Merrill, K. M. 1993, *AJ*, 106, 1906

- Hofner, P., Delgado, H., Whitney, B., Churchwell, E., & Linz, H. 2002, *ApJ*, 579, L95
- Høg, E., et al. 2000, *A&A*, 355, L27
- Howarth, I. D., & Prinja, R. K. 1989, *ApJS*, 69, 527
- Imanishi, K., Koyama, K., & Tsuboi, Y. 2001, *ApJ*, 557, 747
- Jaffe, T. R., Bhattacharya, D., Dixon, D. D., & Zych, A. D. 1997, *ApJ*, 484, L129
- Jiang, Z., et al. 2002, *ApJ*, 577, 245
- Johnson, C. O., Depree, C. G., & Goss, W. M. 1998, *ApJ*, 500, 302
- Johnson, H. L. 1962, *ApJ*, 136, 1135
- Kaastra, J. S. 1992, *An X-Ray Spectral Code for Optically Thin Plasmas* (Internal SRON-Leiden Rep., ver. 2.0)
- Kahn, F. D., & Breitschwerdt, D. 1990, *MNRAS*, 242, 209
- Kassis, M., Deutsch, L. K., Campbell, M. F., Hora, J. L., Fazio, G. G., & Hoffmann, W. F. 2002, *AJ*, 124, 1636
- Kleinmann, D. E. 1973, *Astrophys. Lett.*, 13, 49
- Knödseder, J., Cerviño, M., Le Duigou, J.-M., Meynet, G., Schaerer, D., & von Ballmoos, P. 2002, *A&A*, 390, 945
- Kuznetsov, V. I., Boutenko, G. Z., Lazorenko, G. A., & Lazorenko, P. F. 2000, *A&AS*, 142, 389
- Lada, C. J., Depoy, D. L., Merrill, K. M., & Gatley, I. 1991, *ApJ*, 374, 533
- Lamers, H. J. G. L. M., & Cassinelli, J. P. 1999, *Introduction to Stellar Winds* (Cambridge: Cambridge Univ. Press)
- Landi, E., & Landini, M. 1999, *A&A*, 347, 401
- Leahy, D. A. 1985, *MNRAS*, 217, 69
- Leitherer, C. 1988, *ApJ*, 326, 356
- Leitherer, C., Robert, C., & Drissen, L. 1992, *ApJ*, 401, 596
- Li, J. Z., Wu, C. H., Chen, W. P., Rector, T., Chu, Y. H., & Ip, W. H. 2002, *AJ*, 123, 2590
- Liedahl, D. A., Osterheld, A. L., & Goldstein, W. H. 1995, *ApJ*, 438, L115
- Lyngå, G. 1987, *Computer Based Catalogue of Open Cluster Data* (5th ed.; Strasbourg: CDS)
- Mac Low, M.-M. 2000, *Rev. Mexicana Astron. Astrofis. Ser. Conf.*, 9, 273
- Massey, P., Johnson, K. E., & DeGioia-Eastwood, K. 1995, *ApJ*, 454, 151
- Mathews, W. G. 1966, *ApJ*, 144, 206
- Mathews, W. G., & O'Dell, C. R. 1969, *ARA&A*, 7, 67
- Matsuzaki, K., Sekimoto, Y., Kamae, T., Yamamoto, S., Tatematsu, K., & Umemoto, T. 1999, *Astron. Nachr.*, 320, 323
- McCullough, P. R. 2000, *PASP*, 112, 1542
- McKee, C. F., Van Buren, D., & Lazareff, B. 1984, *ApJ*, 278, L115
- Meaburn, J., & Clayton, C. A. 1987, *MNRAS*, 229, 253
- Meixner, M., Haas, M. R., Tielens, A. G. G. M., Erickson, E. F., & Werner, M. 1992, *ApJ*, 390, 499
- Menzel, D. H. 1937, *ApJ*, 85, 330
- Mewe, R., Lemen, J. R., & van den Oord, G. H. J. 1986, *A&AS*, 65, 511
- Moffat, A. F. J., & Robert, C. 1994, *ApJ*, 421, 310
- Moffat, A. F. J., et al. 2002, *ApJ*, 573, 191
- Morrison, R., & McCammon, D. 1983, *ApJ*, 270, 119
- Morton, D. C. 1967, *ApJ*, 147, 1017
- Muno, M. P., et al. 2003, *ApJ*, 589, 225
- Mytyk, A. M., Daniel, K. J., Gagné, M., & Linsky, J. L. 2001, *AAS Meeting*, 199, 04.08
- Nazé, Y., Chu, Y., Points, S. D., Danforth, C. W., Rosado, M., & Chen, C.-H. R. 2001, *AJ*, 122, 921
- Nielbock, M., Chini, R., Jütte, M., & Manthey, E. 2001, *A&A*, 377, 273
- Nilakshi, Sagar, R., Pandey, A. K., & Mohan, V. 2002, *A&A*, 383, 153
- Oey, M. S., Clarke, C. J., & Massey, P. 2001, in *Dwarf Galaxies and Their Environment*, ed. K. S. de Boer, R.-J. Dettmar, & U. Klein (Aachen: Shaker), 181
- Ogura, K., & Ishida, K. 1976, *PASJ*, 28, 35
- . 1981, *PASJ*, 33, 149
- Oliver, R. J., Masheder, M. R. W., & Thaddeus, P. 1996, *A&A*, 315, 578
- Panagia, N. 1973, *AJ*, 78, 929
- Park, B., & Sung, H. 2002, *AJ*, 123, 892
- Pérez, M. R. 1991, *Rev. Mexicana Astron. Astrofis.*, 22, 99
- Phelps, R. L., & Lada, E. A. 1997, *ApJ*, 477, 176
- Pikel'ner, S. B. 1968, *Astrophys. Lett.*, 2, 97
- Pittard, J. M., Hartquist, T. W., & Dyson, J. E. 2001, *A&A*, 373, 1043
- Pravdo, S. H., Feigelson, E. D., Garmire, G., Maeda, Y., Tsuboi, Y., & Bally, J. 2001, *Nature*, 413, 708
- Preibisch, T., & Zinnecker, H. 2001, *AJ*, 122, 866
- Prinja, R. K., Barlow, M. J., & Howarth, I. D. 1990, *ApJ*, 361, 607
- Rauw, G., Nazé, Y., Gosset, E., Stevens, I. R., Blomme, R., Corcoran, M. F., Pittard, J. M., & Runacres, M. C. 2002, *A&A*, 395, 499
- Rózycka, M., & Tenorio-Tagle, G. 1985, *A&A*, 147, 209
- Seward, F. D., & Chlebowski, T. 1982, *ApJ*, 256, 530
- Schaerer, D., & de Koter, A. 1997, *A&A*, 322, 598
- Schneider, N., Stutzki, J., Winnewisser, G., Poglitsch, A., & Madden, S. 1998, *A&A*, 338, 262
- Schulz, N. S., Canizares, C., Huenemoerder, D., Kastner, J. H., Taylor, S. C., & Bergstrom, E. J. 2001, *ApJ*, 549, 441
- Schulz, N. S., Canizares, C. R., Huenemoerder, D., & Lee, J. C. 2000, *ApJ*, 545, L135
- Smith, R. K., Brickhouse, N. S., Liedahl, D. A., & Raymond, J. C. 2001, *ApJ*, 556, L91
- Snowden, S. L., Egger, R., Finkbeiner, D. P., Freyberg, M. J., & Plucinsky, P. P. 1998, *ApJ*, 493, 715
- Stevens, I. R., & Hartwell, J. M. 2003, *MNRAS*, 339, 280
- Strickland, D. K., Heckman, T. M., Colbert, E. J. M., Hoopes, C. G., & Weaver, K. A. 2003, in *IAU Symp. 212, A Massive Star Odyssey: From Main Sequence to Supernova*, ed. K. A. van der Hucht et al. (San Francisco: ASP), in press
- Strickland, D. K., & Stevens, I. R. 1999, *MNRAS*, 306, 43
- Strömgren, B. 1939, *ApJ*, 89, 526
- Subrahmanyan, R., & Goss, W. M. 1996, *MNRAS*, 281, 239
- Takagi, S., Murakami, H., & Koyama, K. 2002, *ApJ*, 573, 275
- Tenorio-Tagle, G. 1979, *A&A*, 71, 59
- Townsley, L. K., Broos, P. S., Chartas, G., Moskalenko, E., Nousek, J. A., & Pavlov, G. G. 2002a, *Nucl. Instrum. Methods Phys. Res.*, 486, 716
- Townsley, L. K., Broos, P. S., Chu, Y.-H., Feigelson, E. D., Garmire, G. P., Getman, K. V., & Montmerle, T. 2003, *Rev. Mexicana Astron. Astrofis. Ser. Conf.*, 15, 190
- Townsley, L. K., Broos, P. S., Nousek, J. A., & Garmire, G. P. 2002b, *Nucl. Instrum. Methods Phys. Res.*, 486, 751
- Tsvilev, A. P., & Krasnov, V. V. 1999, *Astron. Rep.*, 43, 511
- Tsvilev, A. P., Poppi, S., Cortiglioni, S., Palumbo, G. G. C., Orsini, M., & Maccaferri, G. 2002, *NewA*, 7, 449
- Tsuboi, Y., Koyama, K., Murakami, H., Hayashi, M., Skinner, S., & Ueno, S. 1998, *ApJ*, 503, 894
- Velázquez, P. F., Koenigsberger, G., & Raga, A. C. 2003, *ApJ*, 584, 284
- Walborn, N. R., et al. 2002, *AJ*, 123, 2754
- Wang, Q. D., Gotthelf, E. V., & Lang, C. C. 2002, *Nature*, 415, 148
- Weaver, R., McCray, R., Castor, J., Shapiro, P., & Moore, R. 1977, *ApJ*, 218, 377
- Weisskopf, M. C., Brinkman, B., Canizares, C., Garmire, G., Murray, S., & Van Speybroeck, L. P. 2002, *PASP*, 114, 1
- Welsh, B. Y., Sfeir, D. M., Sallmen, S., & Lallement, R. 2001, *A&A*, 372, 516
- Williams, J. P., Blitz, L., & Stark, A. A. 1995, *ApJ*, 451, 252
- Wolk, S. J., Bourke, T. L., Smith, R. K., Spitzbart, B., & Alves, J. 2002, *ApJ*, 580, L161
- Yusef-Zadeh, F., Law, C., Wardle, M., Wang, Q. D., Fruscione, A., Lang, C. C., & Cotera, A. 2002, *ApJ*, 570, 665